

AD _____

Award Number: W81XWH-09-1-0051

TITLE: Integrated Device for Circulating Tumor Cell Capture, Characterization, and Lens-Free Microscopy

PRINCIPAL INVESTIGATOR: Changhuei Yang

CONTRACTING ORGANIZATION: California Institute of Technology
Pasadena, CA 91125

REPORT DATE: August 2012

TYPE OF REPORT: Final

PREPARED FOR: U.S. Army Medical Research and Materiel Command
Fort Detrick, Maryland 21702-5012

DISTRIBUTION STATEMENT: Approved for public release; distribution unlimited

The views, opinions and/or findings contained in this report are those of the author(s) and should not be construed as an official Department of the Army position, policy or decision unless so designated by other documentation.

REPORT DOCUMENTATION PAGE				Form Approved OMB No. 0704-0188	
Public reporting burden for this collection of information is estimated to average 1 hour per response, including the time for reviewing instructions, searching existing data sources, gathering and maintaining the data needed, and completing and reviewing this collection of information. Send comments regarding this burden estimate or any other aspect of this collection of information, including suggestions for reducing this burden to Department of Defense, Washington Headquarters Services, Directorate for Information Operations and Reports (0704-0188), 1215 Jefferson Davis Highway, Suite 1204, Arlington, VA 22202-4302. Respondents should be aware that notwithstanding any other provision of law, no person shall be subject to any penalty for failing to comply with a collection of information if it does not display a currently valid OMB control number. PLEASE DO NOT RETURN YOUR FORM TO THE ABOVE ADDRESS.					
1. REPORT DATE (DD-MM-YYYY) 01-Aug2012		2. REPORT TYPE Final		3. DATES COVERED (From - To) 1 Aug 2009 - 31 Jul 2012	
4. TITLE AND SUBTITLE Integrated Device for Circulating Tumor Cell Capture, Characterization, and Lens-Free Microscopy				5a. CONTRACT NUMBER	
				5b. GRANT NUMBER W81XWH-09-1-0051	
				5c. PROGRAM ELEMENT NUMBER	
6. AUTHOR(S) Changhuei Yang E-Mail: chyang@caltech.edu; rcote@med.miami.edu				5d. PROJECT NUMBER	
				5e. TASK NUMBER	
				5f. WORK UNIT NUMBER	
7. PERFORMING ORGANIZATION NAME(S) AND ADDRESS(ES) California Institute of Technology Pasadena, CA 91125				8. PERFORMING ORGANIZATION REPORT NUMBER	
9. SPONSORING / MONITORING AGENCY NAME(S) AND ADDRESS(ES) U.S. Army Medical Research and Materiel Command Fort Detrick, Maryland 21702-5012				10. SPONSOR/MONITOR'S ACRONYM(S)	
				11. SPONSOR/MONITOR'S REPORT NUMBER(S)	
12. DISTRIBUTION / AVAILABILITY STATEMENT Approved for Public Release; Distribution Unlimited					
13. SUPPLEMENTARY NOTES					
14. ABSTRACT For this project, we aim to develop and integrate two highly innovative new technologies to capture and characterize circulating tumor cells found in the blood of patients with breast cancer. The first is a highly innovative cell capture technology for blood and other body fluids based on a microfluidics microchip technology. The second is an entirely new imaging technology for performing wide field of viewing microscopy imaging. The resulting device will ultimately be clinically relevant, cost-effective, straight forward, and portable. It will address a significant technology deficiency in current circulating tumor cell analysis at the clinical level that is cost-effective and high-throughput.					
15. SUBJECT TERMS Holography; Holographic optical element; Medical optics and biotechnology; Imaging systems; Scanning microscopy; Optical pathology					
16. SECURITY CLASSIFICATION OF:			17. LIMITATION OF ABSTRACT UU	18. NUMBER OF PAGES 34	19a. NAME OF RESPONSIBLE PERSON USAMRMC
a. REPORT U	b. ABSTRACT U	c. THIS PAGE U			19b. TELEPHONE NUMBER (include area code)

Table of Contents

	<u>Page</u>
Introduction.....	4
Body.....	4
Key Research Accomplishments.....	9
Reportable Outcomes.....	10
Conclusion.....	10
References.....	10
Personnel Report	11
Appendices.....	12

Professor Changhui Yang
California Institute of Technology

Title: Integrated Device for Circulating Tumor Cell Capture, Characterization and Lens-Free Microscopy

Award Number: W81XWH-09-1-0051

Introduction

For this project, we aim to develop and integrate two highly innovative new technologies to capture and characterize circulating tumor cells found in the blood of patients with breast cancer. The first is a highly innovative cell capture technology for blood and other body fluids based on a microfluidics microchip technology. The second is an entirely new imaging technology based on a lens-free holographic scanning. The resulting device will ultimately be clinically relevant, cost-effective, straight forward, and portable. It will address a significant technology deficiency in current circulating tumor cell analysis at the clinical level that is cost-effective and high-throughput.

Project Report:

The aims of the project are:

- Aim 1. Adapt the microfluidics capture device (MFCD) technology for breast cancer CTC capture, identification and characterization.
- Aim 2. Fully evaluate the microscopy imaging needs associated with using MFCD technology for CTC capture, identification and characterization.
- Aim 3. Implement a wide field-of-view (FOV) and high-resolution microscope system based on holographic scanning.
- Aim 4. Combine two components to create a high throughput CTC analysis system.

Aim 1 – 3 were completed by the end of year 2. The focus for the past year has been on Aim 4. At this point, we have completed all aims.

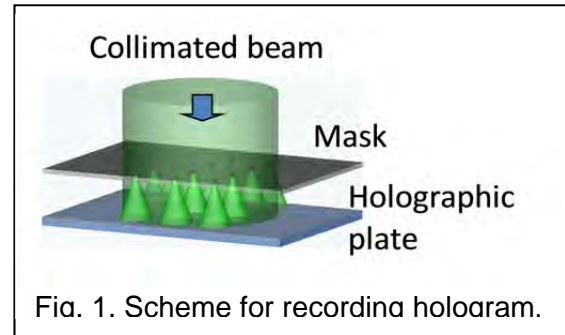
The following report summarizes the project progression in chronological order.

Conceptually, the microscope system we are working on will employ a large grid of tightly focused laser spots to scan our target microscope slide sample. The transmission/fluorescence emission associated with each laser spot interacting with the sample will be collected by a 2D sensor and reconstituted into an image.

The use of this holographic projection approach carries several advantages: 1) We can generate an **arbitrarily large number of sharply focused spots available for scanning** and can thus boost processing speed (current wide FOV systems are constrained by the number of resolvable spots imageable by the associated microscope objectives), 2) **it is cheap to create** large holographic plates for wide field-of-view operation (compared to lens-based large array

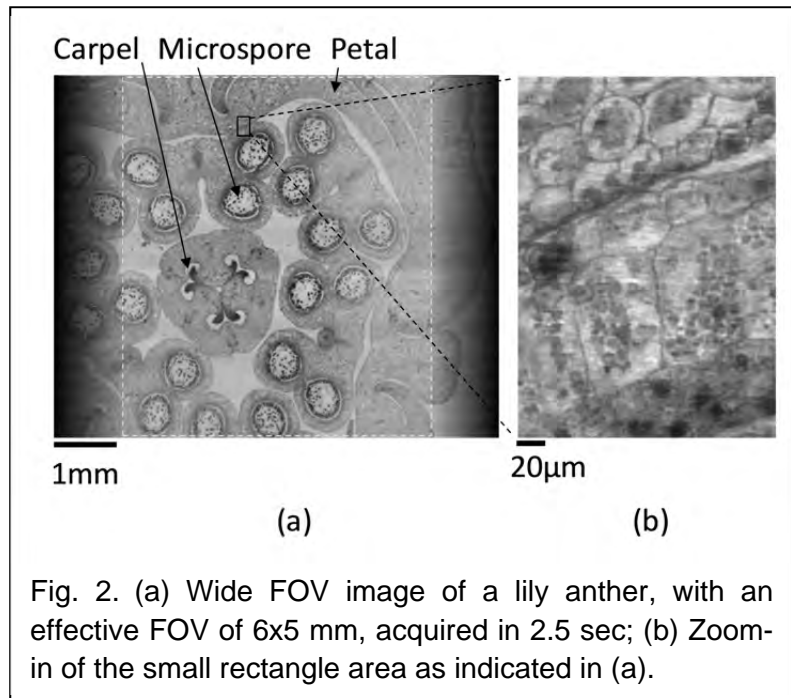
designs), 3) **it allows for flexible focal spot design** (for example, we can implement Bessel beam projection that provides good resolution and long depth of focus), and 4) **it allows for full optoelectronics implementation that eliminates mechanical scanning**. As a specific test of its clinical relevance, we worked with Dr. Cote of U. of Miami to use this technology to image and identify circulating tumor cells (CTCs) that are trapped on the microsieve his group has developed. All these advantages are crucial for addressing the imaging needs for high-throughput screening of the rare CTCs.

In 2010, we successfully demonstrated that it is indeed possible to create a good quality hologram that can generate a grid of tightly focused laser spots. The holographic recording technique we have developed for doing this is highly stable and easy to scale. This approach involves employing a grid of apertures that is patterned on a thinly-metal-coated glass slide as our recording mask. In this case, an incident collimated light beam that is transmitted through the holes will interfere with the fairly strong uniform transmission through the thinly-coated metal layer (in effect, this serves as the write beam) to create a recordable interference pattern. The hologram can be clamped to this mask during recording and, thus, greatly reduce vibrational error. This technique (see Fig. 1) allows us to create holograms of arbitrarily large-format light spot grids with good spot size by simply using a large mask.



Experimentally, we have shown that this approach allows us to create holograms capable of generating light spots of size $0.74\ \mu\text{m}$ (wavelength = $532\ \text{nm}$). The spot size depends on the hologram's ability to record large angle diffractions. Given that our hologram material (Integraf VRP) is spec'ed at 3000 lines/mm, this implies that we should be able to achieve a light spot size of $0.33\ \mu\text{m}$ practically. Experimentally, we have thus far created holographic plates that are capable of generating a grid of light spots at a focal length of 6 mm, FWHM spot size of $0.74\ \mu\text{m}$, separation of $30\ \mu\text{m}$.

We further created a prototype of the target microscope system and employed it to image microscope slides. This prototype consists of an Excelsior-532-200-CDRH laser (wavelength = $532\ \text{nm}$) as the light source, a simple Thorlabs



MAP10100100-A lens pair to project the light transmission from the sample onto a 2D sensor. The sample shown in Fig. 2 consisted of a lily anther slide mounted on a Newport LTA-HS translation stage that was actuated at a speed of 2.5 mm/s during scan. The acquisition time for this transmission image is 2.5 s.

Fig. 3 shows preliminary transmission images of cultured breast tumor cells captured with this prototype.

In 2011, we further implemented a simpler wide FOV imaging scheme that employs a different technique. In this alternate microscope design, the focus grid is generated via the Talbot effect. Here, a mask with an aperture grid is illuminated with a collimated laser beam to produce the focus grid. A 'self-image' of the aperture grid will be reproduced at integer increments of the Talbot distance. This focus



Fig. 3. Image of cultured breast tumor cells.

grid replacement has several advantages. First, the focus grid generation is more repeatable and robust because the mask can be readily fabricated by microfabrication technique. Second, unlike the holographic method, there is no zero-order transmission of the incident beam in the Talbot effect. This will enhance the contrast of the foci on the sensor and thus the signal-to-noise ratio of the image. Third, the focused light spots are more uniform in their powers (spot-to-spot comparison). Finally, this approach allows us to accomplish z-axis scanning (focal plane change) by simply tuning the light source wavelength.

The Talbot effect is a well known phenomenon in which the transmission from a mask with a periodic grid of apertures will reproduce the grid pattern at regular distance intervals from the mask. The distance interval, termed Talbot distance Z_T , can be calculated as

$$Z_T = 2d^2 / \lambda \quad (1)$$

where d is the period of the pattern, and λ is the wavelength. The periodic pattern will reproduce itself at the distance $Z = mZ_T$ or a phase-reversed image at $Z = (m - 1/2)Z_T$, where m is an integer. In principle, any part of this plane can be used as the focused light spot grid for our wide field-of-view microscope. In our experiment, we used the second phase-reversed Talbot plane ($Z_{1.5} = 1.5Z_T$) for more convenient experimental setup.

Interestingly, equation (1) implies that Z_T is inversely proportional to the wavelength. For small tuning of the wavelength, i.e. $\Delta\lambda \ll \lambda$, the Talbot distance change can be calculated as

$$\Delta Z_T = -2d^2 \Delta \lambda / \lambda^2 \quad (2)$$

For a periodicity $d = 30 \mu\text{m}$ and a nominal wavelength of 700 nm , this implies that we can accomplish a significant plane shift of $55 \mu\text{m}$ at $Z = Z_{1.5}$ for a small wavelength change of 10 nm . This tuning ability can be used in our microscope design to accomplish non-mechanical focal plane shift.

Fig. 4 shows images acquired with this new technique and demonstrates its ability to do focal plane shifting by small wavelength detuning.

Over the past year, we have also been developing a flatbed scanner based microscopy imaging approach.

This wide FOV microscopy imaging system uses a low-cost scanner and a closed-circuit-television (CCTV) lens. We show that such an imaging system is capable to capture a $10 \text{ mm} \times 7.5 \text{ mm}$ FOV image with sub-micron resolution, resulting in 0.54 giga-pixels (109 pixels) across the entire image ($26400 \text{ pixels} \times 20400 \text{ pixels}$).

Over the past decades and with the broad acceptance of infinity correction, the conventional

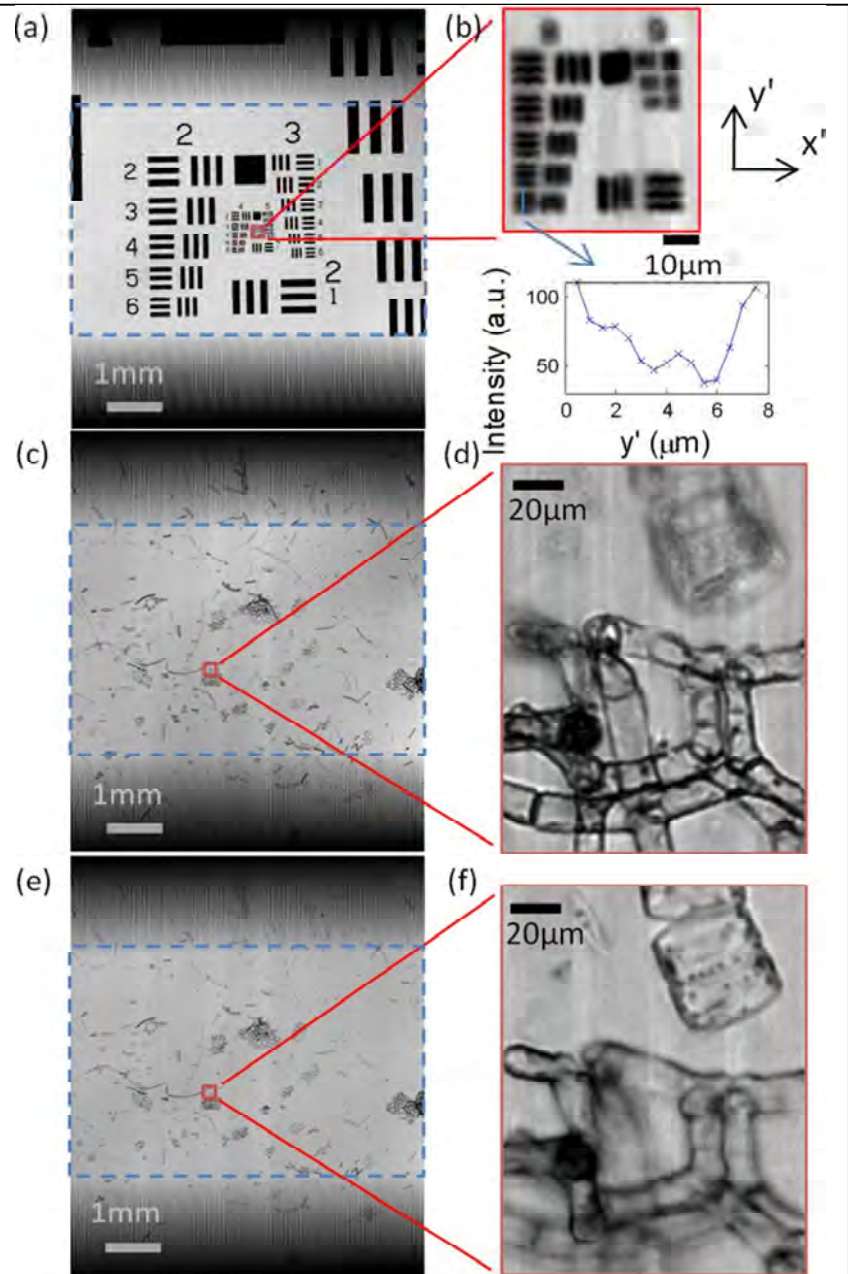


Fig. 4. Images acquired by the Talbot wide field-of-view microscope with effective FOV of $6.4 \times 4.2 \text{ mm}$. (a) Wide FOV image of a U.S. Air Force target, with effective FOV indicated in the large dashed rectangle; (b) Expanded view of the smallest feature of the target and cross-sectional profile of group 8, element 6; (c) Wide FOV image of a mixed green algae slide with wavelength = 692 nm , with effective FOV indicated in the large dashed rectangle; (d) Expanded view of the region indicated in (c); (e) Wide FOV image of a mixed green algae slide with wavelength = 702 nm , with effective FOV indicated in the large dashed rectangle; (f) Expanded view of the region indicated in (e).

microscope design has achieved extensive standardization across the microscopy industry - objectives and eyepieces from the major microscope makers are largely interchangeable. This standardization helps with cost-effectiveness. However, it has also limited the commercial design space for conventional microscopy - any significant design deviation that exceeds the standardization parameter space would have to contend with its incompatibility with the entrenched microscopy consumer base.

The underlying assumptions that underpin all of these developments appear to be 1) a higher space-bandwidth-product (SBP) (the number of independent pixels to characterize the captured image) is about 8 mega-pixels and that increasing this with a magnification-based optical scheme is commercially impractical and 2) the associated pixel count for a radically higher SBP would face electronic image acquisition issues for which a viable solution does not yet exist.

We recently showed that an optical magnification microscopy solution that challenges these assumptions exists. The configuration of this imaging system is based on two cost-effective items: a commercial available closed-circuit-television (CCTV) lens system and a low-cost consumer flatbed scanner. We showed that, such a system is capable to capture a 0.54 giga-pixel microscopy image with a FOV of 10 mm * 7.5 mm and that a sub-micron resolution is achieved across the entire FOV. Remarkably, the CCTV lens system has a SBP of at least 0.5 giga-pixel (10^9 pixels), which is about 2 orders of magnitude larger than those of conventional microscope objectives.

Fig. 5 showed the experimental scheme.

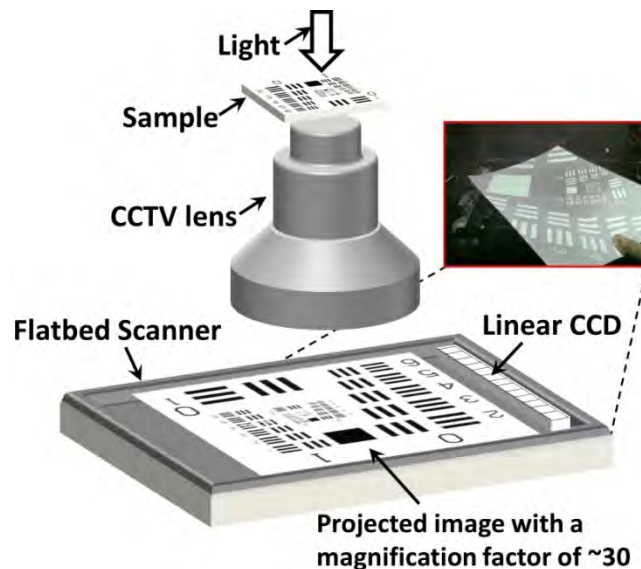


Fig. 5. The setup of the 0.54 giga-pixel microscope (not to scale). A CCTV lens is used to magnify the sample by a factor of 30 and a scanner is used to capture the projected image. The distance between the sample and the lens is about 1 cm. Inset on the top right shows the magnified image of a USAF target on an A4 paper held in front of the scanner.

This solution is simple and easy to implement. Given the specific size of the MFCD, this solution turned out to be very attractive one. We implemented and delivered such a system to Cote's group for use in their execution of their share of the project.

Fig. 6 shows images collected with this system from a MFCD that contains CTCs.

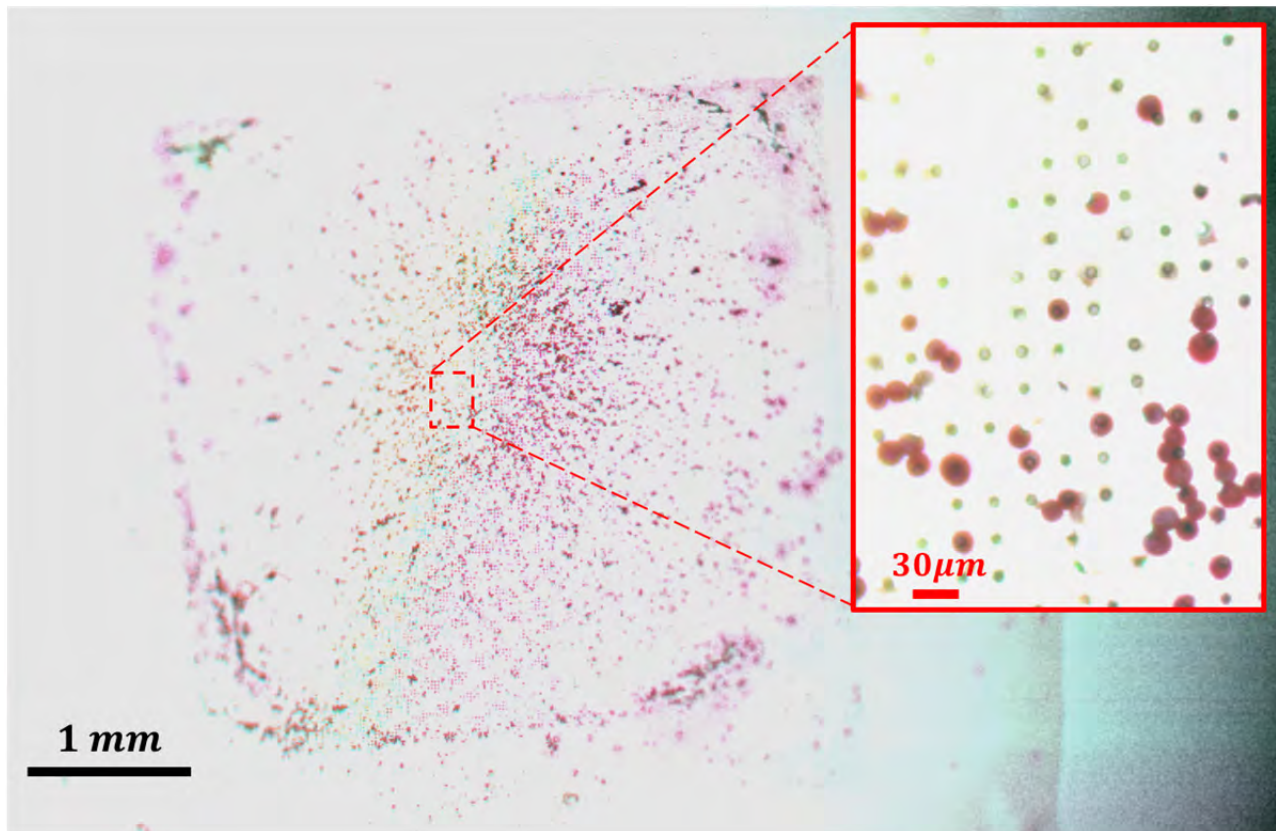


Fig. 6 Color image of the MFCD which contains CTCs (immunohistochemistry stained) collected by the large FOV microscopy system. The inset shows an expanded view of the region indicated by the dashed rectangle.

Key Research Accomplishments:

1. Successfully determined that CTC image identification requires 0.6 micron resolution or better.
2. Fluorescence imaging of CTC requires $\sim 1 \mu\text{M}$ fluorophore concentration sensitivity.
3. Successfully developed a holographic recording process that can record good quality focused light spot grid holograms that can be scaled up easily in size. Larger holograms = larger areas on target slides can be imaged at the same time.
4. Successfully implemented a holographic scanning microscope proof-of-concept with resolution $0.74 \mu\text{m}$ and that is capable of area scanning speed of $12 \text{ mm}^2/\text{s}$.

5. Successfully implemented a Talbot grid scanning microscope with focal depth tuning capability.
6. Successfully implemented a 0.5 gigapixel scanning microscope based on the use of a flatbed scanner and a CCTV lens arrangement.
7. Applied above system to image CTC trapped on a MFCD.

Reportable Outcomes:

1. Jigang Wu, Xiquan Cui, Guoan Zheng, Ying Min Wang, Lap Man Lee, and Changhuei Yang, "Wide field-of-view microscope based on holographic focus grid illumination," Optics Letters 35, 2188-2190 (2010).
2. Jigang Wu, Lap Man Lee and Changhuei Yang, "Focus grid generation by in-line holography," Optics Express 18, 14366-14374 (2010)
3. Patent filed. Xiquan Cui, Changhuei Yang, "Scanning illumination microscope," filed on March 6, 2009
4. Jigang Wu, Guoan Zheng, Zheng Li, and Changhuei Yang, "Focal plane tuning in wide-field-of-view microscope with Talbot pattern illumination," Optics Letters 36 (12), 2179-2181 (2011)
5. Guoan Zheng, Xiaoze Ou, and Changhuei Yang, "0.54 giga-pixel wide-field-of-view microscopy using a flatbed scanner," to be submitted

Conclusion:

Our proof-of-concept prototype demonstrates that the proposed technology is feasible and represents a viable way to process CTCs.

References:

1. Jigang Wu, Xiquan Cui, Guoan Zheng, Ying Min Wang, Lap Man Lee, and Changhuei Yang, "Wide field-of-view microscope based on holographic focus grid illumination," Optics Letters 35, 2188-2190 (2010).
2. Jigang Wu, Lap Man Lee and Changhuei Yang, "Focus grid generation by in-line holography," Optics Express 18, 14366-14374 (2010)
3. Jigang Wu, Guoan Zheng, Zheng Li, and Changhuei Yang, "Focal plane tuning in wide-field-of-view microscope with Talbot pattern illumination," Optics Letters 36 (12), 2179-2181 (2011)

4. Guoan Zheng, Xiaoze Ou, and Changhuei Yang, "0.54 giga-pixel wide-field-of-view microscopy using a flatbed scanner," to be submitted

Personnel Report:

The following table shows all personnel that received pay for this research effort.

Name	Degree	Role on Project	Months on Project
Changhuei Yang	PhD	PI	Oct 2009 – Jun 2012
Jigang Wu	PhD	Postdoctoral Scholar, Staff Scientist	Oct 2009 – Apr 2011
Seung Ah Lee	Candidate PhD	Graduate Research Assistant	Oct 2010 – Jan 2011
Zheng Li	MS	Graduate Research Assistant	Mar 2011 – Dec 2011

Wide field-of-view microscope based on holographic focus grid illumination

Jigang Wu,^{1,*} Xiquan Cui,¹ Guoan Zheng,¹ Ying Min Wang,² Lap Man Lee,² and Changhui Yang^{1,2}

¹Department of Electrical Engineering, California Institute of Technology, 1200 E. California Boulevard, Pasadena, California 91125, USA

²Department of Bioengineering, California Institute of Technology, 1200 E. California Boulevard, Pasadena, California 91125, USA

*Corresponding author: jigang@caltech.edu

Received March 22, 2010; revised May 19, 2010; accepted May 29, 2010;
posted June 7, 2010 (Doc. ID 125762); published June 23, 2010

We have developed a new microscopy design that can achieve wide field-of-view (FOV) imaging and yet possesses resolution that is comparable to a conventional microscope. In our design, the sample is illuminated by a holographically projected light-spot grid. We acquire images by translating the sample across the grid and detecting the transmissions. We have built a prototype system with an FOV of $6\text{ mm} \times 5\text{ mm}$ and acquisition time of 2.5 s. The resolution is fundamentally limited by the spot size—our demonstrated average FWHM spot diameter was $0.74\text{ }\mu\text{m}$. We demonstrate the prototype by imaging a U.S. Air Force target and a lily anther. This technology is scalable and represents a cost-effective way to implement wide FOV microscopy systems. © 2010 Optical Society of America

OCIS codes: 170.0110, 090.2890, 170.5810.

Automated, high-resolution, and cost-effective wide field-of-view (FOV) microscopy is highly sought for many applications, such as high-throughput screening [1] and whole-slide digital pathology diagnosis [2]. In a conventional microscope, the FOV is inversely related to the microscope objective's resolution due to the critical requirement of aberration correction for the whole viewing area. Commercial products for accomplishing wide FOV imaging typically raster scan the target samples under microscope objectives and reconstitute full-view images from multiple smaller images. This approach requires precise mechanical actuation along two axes. Scaling up the FOV for such an approach requires a linear cost increase (add more objectives) or longer scan time. Recently, exciting in-line holography methods [3,4] demonstrated the potential to cover a wide FOV image very cost effectively and without requiring sophisticated optics and mechanical scanning. In-line holography does require excellent raw data quality, as data noise can significantly distort the computed image and deteriorate resolution. To our knowledge, in-line holography's demonstrated resolution for simple objects is about $1\text{ }\mu\text{m}$ [3].

In this Letter, we report a microscopy technique that employs holography concepts in a different fashion to accomplish wide FOV imaging. Our technique, termed holographic scanning microscopy (HSM), uses a specially written hologram to generate a grid of tightly focused light spots and uses this grid as illumination on the target sample to perform parallel multifocal scanning while the sample is translated across the grid. In comparison to in-line holography, the resolution here is fundamentally determined by the focused spot size. Unlike in-line holography, this approach does not require mechanical scanning, but the scanning format is a simple one-dimensional (1D) translation. This approach is readily scalable, as we would simply use a large hologram with more projection light spots to accomplish wider FOV imaging.

Our HSM prototype demonstration, as shown in Fig. 1(a), used a laser (Excelsior-532-200-CDRH, Spectra Physics, with wavelength of 532 nm and power of 200 mW) as light source. The laser was attenuated, spatial

filtered, and expanded to be a collimated Gaussian beam with $1/e^2$ beam diameter of 21.3 mm. We used the center portion of the beam (diameter 12 mm and power 1 mW) as the illumination. A hologram transferred the incoming collimated beam into a grid of 200×40 (along the x and the y direction, respectively) focused light spots at a focal length of 6 mm. The spacing between spots was $30\text{ }\mu\text{m}$. The sample was mounted on a translation stage (LTA-HS, Newport) and positioned under the illumination of the focus grid. An achromatic lens pair (MAP10100100-A, Thorlabs) imaged the focus grid onto the imaging sensor (MotionXtra N3 with 1280×1024 pixels and $12\text{ }\mu\text{m}$ pixel size, Integrated Design Tools) with a magnification of 1.6. Note that the aberration induced in the projection lenses is not critical since we only need to differentiate different focus spots, which were well separated ($30\text{ }\mu\text{m}$). A beam block with diameter of 1 mm was positioned at the focus of the lens pair to block the zero-order transmission through the hologram.

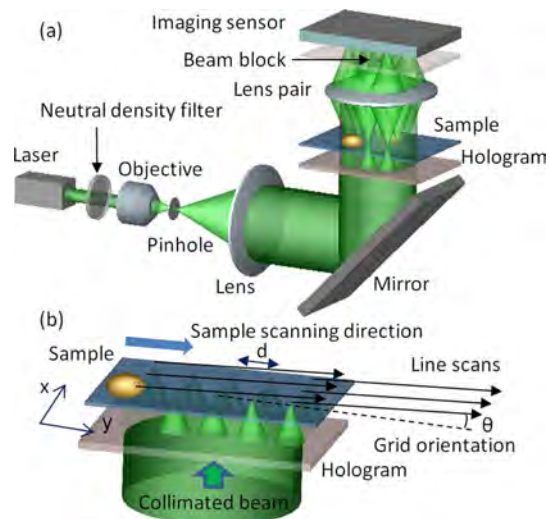


Fig. 1. (Color online) (a) System setup of the wide FOV microscope system and (b) scanning mechanism employed for imaging.

In the experiment, we linearly scanned the sample across the focus grid, which was tilted at a small angle with respect to the scanning direction, as shown in Fig. 1(b), and detected the transmission of the foci through the sample. Each focus spot will contribute to a line scan of the sample and a microscopic image can be reconstructed by appropriately shifting and assembling the line scans. This scanning scheme is similar to that of the optofluidic microscope [5], except that here we used a two-dimensional focus grid instead of a 1D aperture array. The focus grid was arranged so that the line scans of the adjacent columns of spots can be directly patched together. The linear scanning scheme has two advantages. First, we can achieve a small sampling distance of the image with relatively large focus spot spacing because of the slight angular tilt geometry. Second, it is simpler and can be much faster than a raster scanning scheme. As shown in Fig. 1(b), the sampling distances in the x and y directions can be written as

$$\delta x = d \sin(\theta), \quad \delta y = v/F, \quad (1)$$

where d is the spacing between focus spots, θ is the tilt angle of the focus grid with respect to the sample scanning direction, v is the scanning speed, and F is the frame rate of the imaging sensor. In the experiment, we chose the parameters to be $d = 30 \mu\text{m}$, $\theta = 0.025 \text{ rad}$, $v = 2.5 \text{ mm/s}$, and $F = 3333 \text{ frames/s}$. The exposure time was $7 \mu\text{s}$. Thus the sampling distances δx and δy were both $0.75 \mu\text{m}$, approximately matching the average focus spot size in our HSM system. Note that a high density of focused light spots is desirable as it would allow us to simultaneously collect more image data. On the other hand, we need to maintain adequate separation between adjacent light spots so that their projections on the sensor can be unambiguously distinguished. Our chosen spacing of $30 \mu\text{m}$ worked well as a compromise.

According to the scanning scheme, the FOV in the x direction is determined by the extent of focus spots in this direction. Because of the linear scanning characteristics, the starting and ending part of the image will have a sawtooth shape, as shown in Fig. 1(b). The effective FOV in the y direction can be calculated by $L - H$, where L is the scan length and H is the extent of focus spots in the y direction. We used 200×40 focused light spots with $30 \mu\text{m}$ spacing, and a scan length of 6.2 mm for acquiring our images. Thus the FOV in the x direction was 6 mm in the x direction and 5 mm in the y direction. The acquisition time of the image is determined by the scanning speed and the range of the translation stage, and was calculated to be 2.5 s . We note that the FOV in the x direction can be expanded by simply adding more focused light spots along that direction through the use of a larger hologram. The FOV in the y direction is limited only by the extent to which we are willing to translate our sample along that direction.

The key optical component of our HSM system is the hologram. The use of holography to generate tiny focus spots has been reported in the literature [6,7]. Our hologram is technically challenging, as we require it to be capable of rendering tightly focused light spots over a relatively wide area. We implemented a scheme that is capable of patterning such a hologram [shown in Fig. 2(a)]. In this scheme, we employed a specially prepared mask. The mask consisted of a grid of apertures

patterned on a layer of metal film. The aperture diameter was $0.8 \mu\text{m}$, and the spacing between adjacent apertures was $30 \mu\text{m}$. The metal film was intentionally chosen to be thin (with an optical density of ~ 3) so that the incoming collimated light can be transmitted through it and be attenuated. The light transmitted through the apertures, serving as the sample beam, would then interfere with the attenuated collimated light, serving as the reference beam, and project an appropriate pattern onto the holographic plate (VRP, Integraf) for recording.

After exposure, the holographic plate was developed and bleached to produce the hologram. During reconstruction, as shown in Fig. 2(b), a conjugated collimated beam can then be transformed into a focus grid, and the focal length is the same as the distance between the holographic plate and the mask during recording. Note that there is a strong zero-order beam during reconstruction that needs to be blocked to enhance the spot pattern contrast in the imaging sensor, as shown in Fig. 1(a). Using the in-line holography scheme, the focal length can be adjusted easily, and a large area of apertures in the mask can be recorded. The effective NA of the recording is ultimately limited by the resolution of the holographic material. Our holographic plate has a resolution of more than 3000 lines/mm , which corresponds to a maximum NA of 0.8 . The focus grid was observed under a microscope to measure the focus spot size. Figures 2(d)–2(f) show microscope images, using a $60\times$ objective, of spots from different region of the focus grid, as indicated in Fig. 2(c). The FWHM spot size was measured to be $0.65\text{--}0.80 \mu\text{m}$ (average of $0.74 \mu\text{m}$). The effective NA was ~ 0.36 , and the Rayleigh range is $\sim 2.3 \mu\text{m}$. The deviation of the experimental NA from the theoretical maximum NA is attributable to recording and developing imperfections. The nonuniform spot intensities of different focus spots were compensated by a normalization procedure during data processing. Note that the spot size in the x direction is larger than that in the y direction. The asymmetric shape of the spot was due to slight misalignment of the mask and holographic plate during the recording process.

The simplicity of this recording scheme and its robustness are important, as the method can be used to create

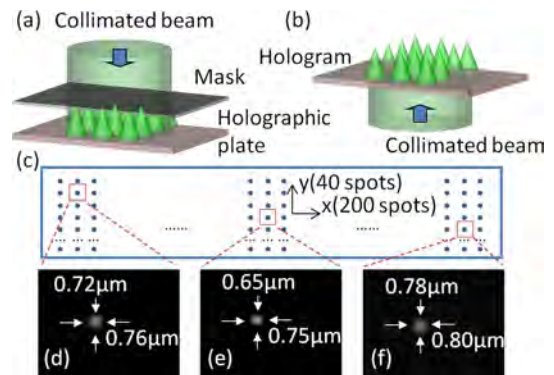


Fig. 2. (Color online) (a) In-line holographic recording scheme for making the hologram, (b) generation of focus grid illumination by holographic reconstruction using the hologram, (c) schematic of the focus grid, and (d)–(f) observation of focus spots from different regions of the focus grid, as indicated in (c), under a microscope using a $60\times$ objective.

large format and good quality light-spot-grid holograms. At this point, it is also worth noting that there are other ways to implement focus grid illumination, e.g., by using a microlens array [8]. The challenge of using a microlens array lies in the fact that, to maintain a reasonable NA and high focus-light-spot density, the focal length would have to be very short. For example, for a spacing of $30\text{ }\mu\text{m}$ and NA of 0.36, the microlens would have a diameter of $30\text{ }\mu\text{m}$ and a focal length of $\sim 40\text{ }\mu\text{m}$. Aside from fabrication issues related to the difficulty of implementing such small lenses and short focal lengths with good focusing quality, the short focal length is also inconvenient for sample handling. In comparison, our hologram had a much longer focal length of 6 mm. This difference is attributable to the fact that the effective lenses in the hologram can overlap each other, while microlenses simply cannot overlap in a microlens array. In fact, the extent of overlap for our prototype was remarkable. In our prototype, the holographic “lenses” were effectively 4.3 mm in diameter, while the lens-center spacing was $30\text{ }\mu\text{m}$.

To test our prototype system, we acquired images of a U.S. Air Force target and a lily anther microscope slide, as shown in Fig. 3. Figure 3(a) shows the wide FOV image of the U.S. Air Force target with effective FOV indicated by a dashed rectangle. Figure 3(b) shows the expanded view of the region indicated in Fig. 3(a), which contains the smallest feature size with a line width of $2.2\text{ }\mu\text{m}$ (group 7, element 6). Figure 3(c) shows the wide FOV image of the lily anther. Many distinct features, such as carpel, microspore, and petal, of the lily anther can be seen in the image. Small features can also be discerned, as demonstrated in Fig. 3(d), where an expanded-view image of the rectangle area indicated in Fig. 3(c) is shown. We can see that our system can render a wide FOV image and still provide good resolution. The shadow artifacts that are apparent in Fig. 3(b) were caused by crosstalk among the projected transmissions of the light spots. Light spots that were close to the feature edges tend to diffract strongly and introduce light onto regions of the camera that are sampling other spots. These systemic artifacts can be iteratively corrected via postimaging processing. We also note that scan motion nonuniformity ($\sim 0.8\text{ }\mu\text{m}$) is the cause of the image jitter along the scan direction, as can be seen in some horizontal bars. This issue can be solved by employing a more uniform linear actuation system.

Our HSM prototype actually operates in a sub-Nyquist sampling regime. To render full images at the fundamental resolution limit set by the spot size, the sampling increment for both directions should be halved. This can be accomplished by choosing a tilt angle θ of 0.0125 rad and using a scanning speed v of 6666 frames/s. Our achieved resolution with the demonstration operating parameters was $1.5\text{ }\mu\text{m}$; this is why we were able to discern the smallest individual scale bars (feature width = $2.2\text{ }\mu\text{m}$) in Fig. 3(b).

We note that our system does not contain feedback systems (common in commercial FOV systems) for keeping the sample in focus during scanning. We believe that our HSM design can potentially allow us to solve the axial focus control issue by a different means—by using the hologram to instead project a grid of finite Bessel beams [9], we can potentially image nonflat samples without requiring focus tracking. Finally, we note that the HSM can

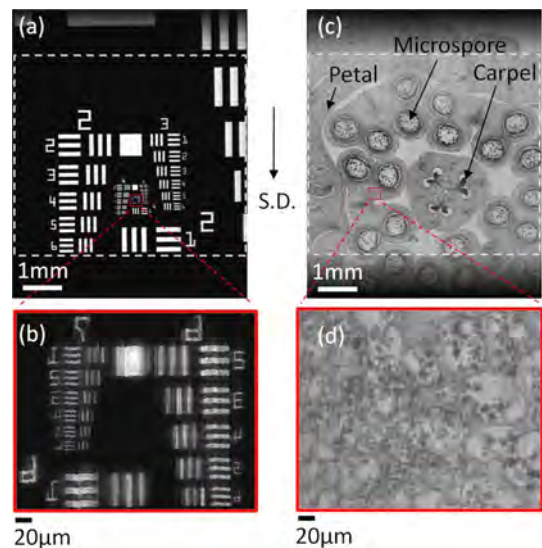


Fig. 3. (Color online) (a) Wide FOV image of a U.S. Air Force target, with an effective FOV of $6\text{ mm} \times 5\text{ mm}$, as indicated in the large dashed rectangle, (b) expanded view of the smallest feature (groups 6 and 7) of the target, as indicated in (a), (c) wide FOV image of a lily anther, with an effective FOV of $6\text{ mm} \times 5\text{ mm}$, as indicated in the large dashed rectangle, and (d) expanded view of the small rectangle area as indicated in (c). S.D., scanning direction.

potentially collect fluorescence images by simply inserting the appropriate filter.

In summary, we have shown a wide FOV microscope system based on holographic focus grid illumination. The use of focus grid illumination can effectively provide wide FOV and high-resolution microscopy imaging. We have demonstrated the principle by making a prototype system with an FOV of $6\text{ mm} \times 5\text{ mm}$ and an acquisition time of 2.5 s. The resolution is fundamentally limited by the spot size—our demonstrated average FWHM spot diameter was $0.74\text{ }\mu\text{m}$. The prototype system was used to image a U.S. Air Force target and a lily anther for capability testing.

This work is supported by Department of Defense grant W81XWH-09-1-0051. The authors acknowledge Richard Cote and Ram Datar from the University of Miami for helpful discussions.

References

1. M. Oheim, *Br. J. Pharmacol.* **152**, 1 (2007).
2. J. Ho, A. V. Parwani, D. M. Jukic, Y. Yagi, L. Anthony, and J. R. Gilbertson, *Hum. Pathol.* **37**, 322 (2006).
3. W. B. Xu, M. H. Jericho, I. A. Meinertzhagen, and H. J. Kreuzer, *Proc. Natl. Acad. Sci. USA* **98**, 11301 (2001).
4. S. Seo, T. W. Su, D. K. Tseng, A. Erlinger, and A. Ozcan, *Lab Chip* **9**, 777 (2009).
5. X. Q. Cui, L. M. Lee, X. Heng, W. W. Zhong, P. W. Sternberg, D. Psaltis, and C. H. Yang, *Proc. Natl. Acad. Sci. USA* **105**, 10670 (2008).
6. W. H. Liu and D. Psaltis, *Opt. Lett.* **24**, 1340 (1999).
7. F. Kalkum, S. Broch, T. Brands, and K. Buse, *Appl. Phys. B* **95**, 637 (2009).
8. C. H. Sow, A. A. Bettiol, Y. Y. G. Lee, F. C. Cheong, C. T. Lim, and F. Watt, *Appl. Phys. B* **78**, 705 (2004).
9. J. Durnin, J. J. Miceli, and J. H. Eberly, *Opt. Lett.* **13**, 79 (1988).

Focus grid generation by in-line holography

Jigang Wu,^{1,*} Lap Man Lee,² and Changhui Yang^{1,2}

¹*Department of Electrical Engineering, California Institute of Technology, 1200 E California Blvd., Pasadena, CA 91125, USA*

²*Department of Bioengineering, California Institute of Technology, 1200 E California Blvd., Pasadena, CA 91125, USA*

**jigang@caltech.edu*

Abstract: We describe a simple way to generate a wide-area high-resolution focus grid by in-line holography and study the factors that impacts its quality. In our holographic recording setup, the reference beam was the direct transmission of the incoming collimated laser beam through a mask coating with thin metal film, and the sample beam was the transmission of the laser through small apertures fabricated on the mask. The interference of the two beams was then recorded by a holographic plate positioned behind the mask. Compared with other recording schemes, the in-line holography scheme has many distinct advantages and is more suitable for generating a wide-area focus grid. We explored the dependence of diffraction quality, including reconstructed focus spot intensity and spot size, on different parameters for recording, such as optical density of the metal film, size of the apertures, and focal lengths. A wide-area focus grid (170 x 138 spots with area 5.1 mm x 4.1 mm) was recorded using the in-line holography scheme for a demonstration.

©2010 Optical Society of America

OCIS codes: (090.0900) Holography; (090.2890) Holographic optical element.

References and links

1. R. Gräf, J. Rietdorf, and T. Zimmermann, "Live cell spinning disk microscopy," *Adv. Biochem. Eng. Biotechnol.* **95**, 57–75 (2005).
 2. J. Bowersdorf, R. Pick, and S. W. Hell, "Multifocal multiphoton microscopy," *Opt. Lett.* **23**(9), 655–657 (1998).
 3. P. M. Lundquist, C. F. Zhong, P. Zhao, A. B. Tomaney, P. S. Peluso, J. Dixon, B. Bettman, Y. Lacroix, D. P. Kwo, E. McCullough, M. Maxham, K. Hester, P. McNitt, D. M. Grey, C. Henriquez, M. Foquet, S. W. Turner, and D. Zaccarin, "Parallel confocal detection of single molecules in real time," *Opt. Lett.* **33**(9), 1026–1028 (2008).
 4. J. Ho, A. V. Parwani, D. M. Jukic, Y. Yagi, L. Anthony, and J. R. Gilbertson, "Use of whole slide imaging in surgical pathology quality assurance: design and pilot validation studies," *Hum. Pathol.* **37**(3), 322–331 (2006).
 5. M. Oheim, "High-throughput microscopy must re-invent the microscope rather than speed up its functions," *Br. J. Pharmacol.* **152**(1), 1–4 (2007).
 6. J. Wu, X. Cui, G. Zheng, Y. M. Yang, L. M. Lee, and C. Yang, "A wide field-of-view microscope based on holographic focus grid illumination," (accepted by *Opt. Lett.*).
 7. F. Kalkum, S. Broch, T. Brands, and K. Buse, "Holographic phase conjugation through a sub-wavelength hole," *Appl. Phys. B* **95**(3), 637–645 (2009).
 8. W. Liu, and D. Psaltis, "Pixel size limit in holographic memories," *Opt. Lett.* **24**(19), 1340–1342 (1999).
 9. D. Gabor, "A new microscopic principle," *Nature* **161**(4098), 777–778 (1948).
 10. J. J. Barton, "Removing multiple scattering and twin images from holographic images," *Phys. Rev. Lett.* **67**(22), 3106–3109 (1991).
 11. W. Xu, M. H. Jericho, I. A. Meinertzhagen, and H. J. Kreuzer, "Digital in-line holography for biological applications," *Proc. Natl. Acad. Sci. U.S.A.* **98**(20), 11301–11305 (2001).
 12. V. Moreno, J. F. Roman, and J. R. Salgueiro, "High efficiency diffractive lenses: deduction of kinoform profile," *Am. J. Phys.* **65**(6), 556–562 (1997).
 13. M. H. Horman, and H. H. M. Chau, "Zone plate theory based on holography," *Appl. Opt.* **6**(2), 317–322 (1967).
 14. J. W. Goodman, *Introduction to Fourier Optics* (Roberts & Company Publishers, 3rd edition, 2004), Chap. 9.
 15. C. Genet, and T. W. Ebbesen, "Light in tiny holes," *Nature* **445**(7123), 39–46 (2007).
 16. A. K. Richter, and F. P. Carlson, "Holographically generated lens," *Appl. Opt.* **13**(12), 2924–2930 (1974).
 17. H. I. Bjelkhagen, *Silver-halide recording materials for holography and their processing* (Springer, 2nd edition, 1995), Chap. 5.
-

1. Introduction

Focus grid illuminations has been used for multi-beam confocal microscopy [1], multifocal microscopy [2], and single molecule detection [3], etc. In such applications, it is important to generate a tight focus spot for high-resolution imaging, and a small spacing between the focus spots for fast image acquisition speed. Previously, the focus grid is usually generated by using microlens array, diffractive optical elements, or holographic optical elements, along with a microscope objective to achieve the abovementioned characteristics. One disadvantage of these methods is that the area of the focus grid illumination will be limited by the field-of-view of microscope objective, and is thus unsuitable for applications that require wide field-of-view imaging, e.g., whole-slide imaging [4] or high-throughput imaging and sensing [5]. Obviously, to achieve a wider field-of-view, the microscope objective has to be eliminated when generating the focus grid illumination.

An appropriately designed microlens array provides a good alternate solution. The number of elements in such an array can be scaled up arbitrarily. However, there is a significant downside to such a solution – the grid density is typically low. This is because the required numerical apertures for high resolution spots ($< 1\ \mu\text{m}$) necessarily require the focus spot separation and the focal length to be high. For example, to accomplish a focused spot size of $1\ \mu\text{m}$ at a focal distance of $10\ \text{mm}$, each microlens in the array would have to be at least $5\ \text{mm}$ in diameter (assuming wavelength of $500\ \text{nm}$). Since the pitch of the focus grid is equal to microlens' diameter, this implies that such an array would have a pitch of $5\ \text{mm}$. This sparse grid density is a significant impediment for most applications. The grid density can potentially be increased by using smaller lenses with shorter focal lengths. However, the required optical surfaces would be more difficult to fabricate and the shorter focal lengths may be restrictive for certain applications.

Interestingly, it is worth noting that the physical lenses are not the only means by which we can focus light. It is also possible to implement a virtual microlens array via holographic recording. An appropriately patterned piece of holographic plate should be able to transform a uniform input coherent light field into a grid of tightly focused light spots. The holographic projection-base approach has two advantages. First, implementation would be simpler and cheaper, as long as we can write the appropriate pattern into the holographic plate. Second, the effective holographic lenses can 'overlap' to a great extent, and, as such, we would be able to achieve a higher focus grid density. Recently, we showed that an appropriately patterned holographic plate can generate light spots of diameter $0.74\ \mu\text{m}$ at a focal distance of $6\ \text{mm}$ with a pitch of $30\ \mu\text{m}$ [6]. The corresponding holographic lens diameter is $4.3\ \text{mm}$. This implies that the lens overlap ratio (lens diameter divided by pitch) is 140 (for conventional lenslet array, this ratio is at most 1).

The use of holography to generate a high-resolution focus spot has been demonstrated by several groups via well-designed schemes [7, 8]. In their schemes, the transmission of a tiny aperture was interfered with a reference beam and recorded by holographic materials. This approach can provide high-quality and well-controlled recording.

In-line holography was originally proposed by Gabor more than half a century ago [9] and has been studied extensively since then [10, 11]. In this paper, we show that an in-line holography scheme can be used for generating a wide-area focus grid. In our scheme, as shown in Fig. 1(a), the direct transmission of a collimated laser beam through a semi-transparent mask interferes with the transmission of the laser through an aperture grid fabricated on the semi-transparent mask, and the interference pattern is recorded by a holographic plate. The advantages of our scheme can be summarized as follows: (1) The in-line scheme make the setup insensitive to vibrations and perturbations in the system; (2) The focal length of the focus grid can be adjusted easily and can be short with relative ease; (3) The scheme is suitable for recording large-area aperture grid and thus suitable for achieving large-area focus grid. This paper reports our experimental findings regarding the impact of various implementation parameters on the quality of the recording.

The quality of the holographic recording depends on the aperture size, the opacity of the mask and the focal length. The parameter choices for creating an optimal recording are not apparent by simply dissecting the problem analytically. Here, we experimentally show the impact of each major design choice on the recording's properties. This paper will hopefully serve as a guide for researchers looking to create such holographic grids for their respective experiments.

In section 2, we will describe the in-line holography setup for recording the hologram for generating a focus grid and present a theory for calculating the reconstructed focus spot intensity. In section 3, we show a series of experiment that studies the dependence of hologram quality, including reconstructed spot size and diffraction efficiency, on experiment parameters, such as optical density (OD) of the mask, the aperture size, and the focal length. Finally, we summarize our work in section 4.

2. In-line holography setup

The in-line holography setup for recording a hologram that can generate a focus spot (a holographic lens) is shown in Fig. 1(a). The holographic lens is also called a sinusoidal zone plate [12] or a Garbor zone plate [13]. The mask in the setup consists of an aperture patterned on a layer of metal film. When a collimated laser beam shines on the mask, the transmission through the aperture serves as sample wave. The metal film is deliberately made to be thin so that the collimated laser beam can directly transmit through it and be attenuated. The direct transmission of the beam through the metal film then serves as reference wave and interferes with the sample beam and the interference is recorded by a holographic plate positioned at a certain distance behind the mask. In the experiment, we used a silver halide holographic plate.

After exposure, the holographic plate was developed and bleached to produce a phase hologram. A focus spot can then be generated by the holographic reconstruction process, as shown in Fig. 1(b), where a conjugated collimated beam is transformed into a focus spot by the hologram. The focal length of the holographic lens is the same as the distance between the mask and the holographic plate during the recording process.

By replacing the mask with one that is patterned with a grid of apertures, the same process will yield a phase hologram that can render a grid of focus spots.

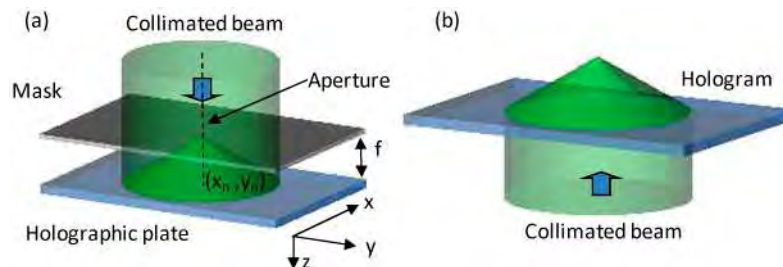


Fig. 1. In-line holography scheme for fabricating a holography lens. (a) Recording of the hologram; (b) Reconstruction of the focus spot.

Considering the sensitivity dynamic range of holographic materials, it is preferable to make the intensity of reference beam comparable to that of the sample beam. This is true if we have only one aperture on the mask. However, for aperture grid on the mask, the interference between the transmissions of different apertures will contribute to the hologram pattern and affect diffraction if the transmissions are comparable to the reference beam transmission. Thus in the recording scheme, it is important to make the intensity of the reference beam much stronger than that of the sample beam so that a reasonable reconstruction can be achieved [14].

The transmission through tiny apertures is generally a complicated problem and defies simple solution without some approximations [15]. An approximate theory for calculating holographically generated lens can be found in Ref [16], where the Fraunhofer diffraction was used to approximate the transmission through the aperture. Similar to Ref [13], our

calculation below is based on the simpler assumption that the sample beam is a combination of spherical waves and the reference beam is a plane wave, since the apertures in our experiment is comparable to the wavelength and much smaller than the focal length. Using paraxial approximation, the sample wave, i.e., the transmission through the aperture grid, can be written as

$$\frac{A_1}{f} \sum_n \exp\left(i \frac{\pi}{f\lambda} [(x-x_n)^2 + (y-y_n)^2]\right) \quad (1)$$

where f is the focal length, A_1/f is the amplitude of one hole, (x_n, y_n) is the coordinate of the center of the aperture n , and λ is the laser wavelength. Here we neglect the constant phase shift from propagation along z -direction. Figure 1(a) shows the scheme with aperture n . Thus the interferogram intensity on the holographic plate can be written as:

$$\begin{aligned} I(x) &\approx \left| A_0 + \frac{A_1}{f} \sum_n \exp\left(i \frac{\pi}{f\lambda} [(x-x_n)^2 + (y-y_n)^2]\right) \right|^2 \\ &= A_0^2 + 2A_0 \frac{A_1}{f} \sum_n \cos\left(\frac{\pi}{f\lambda} [(x-x_n)^2 + (y-y_n)^2]\right) \\ &\quad + \frac{A_1^2}{f^2} \sum_n \exp\left(i \frac{\pi}{f\lambda} [(x-x_n)^2 + (y-y_n)^2]\right) \sum_n \exp\left(-i \frac{\pi}{f\lambda} [(x-x_n)^2 + (y-y_n)^2]\right) \\ &\approx A_0^2 + 2A_0 \frac{A_1}{f} \sum_n \cos\left(\frac{\pi}{f\lambda} [(x-x_n)^2 + (y-y_n)^2]\right) \end{aligned} \quad (2)$$

where A_0 is reference wave amplitude. Here we use the approximation that $A_1 \ll A_0$.

After developing and bleaching, we will get a phase hologram [17] and the transmission can be written as

$$\begin{aligned} t(x) &= \exp\left[iK \left(A_0^2 + 2A_0 \frac{A_1}{f} \sum_n \cos\left(\frac{\pi}{f\lambda} [(x-x_n)^2 + (y-y_n)^2]\right) \right)\right] \\ &= \exp(iKA_0^2) \prod_n \exp\left[i\beta \cos\left(\frac{\pi}{f\lambda} [(x-x_n)^2 + (y-y_n)^2]\right)\right] \end{aligned} \quad (3)$$

where K is a constant, and $\beta = 2KA_0A_1/f$ is the modulation amplitude. The modulation term can be further expanded as

$$\exp\left[i\beta \cos\left(\frac{\pi}{f\lambda} [(x-x_n)^2 + (y-y_n)^2]\right)\right] = \sum_{l=-\infty}^{\infty} (i)^l J_l(\beta) \exp\left[i l \frac{\pi}{f\lambda} [(x-x_n)^2 + (y-y_n)^2]\right] \quad (4)$$

where $J_l(\beta)$ is the l th order Bessel function of the first kind. When β is small and $l \geq 0$,

$$J_l(\beta) \approx \frac{1}{\Gamma(l+1)} \left(\frac{\beta}{2}\right)^l \quad (5)$$

Neglecting higher order terms, we have

$$\begin{aligned}
& \exp \left[i\beta \cos \left(\frac{\pi}{f\lambda} [(x-x_n)^2 + (y-y_n)^2] \right) \right] \\
& \approx J_0(\beta) + iJ_1(\beta) \exp \left[i \frac{\pi}{f\lambda} [(x-x_n)^2 + (y-y_n)^2] \right] + iJ_{-1}(\beta) \exp \left[-i \frac{\pi}{f\lambda} [(x-x_n)^2 + (y-y_n)^2] \right] \quad (6) \\
& \approx 1 + \frac{i\beta}{2\Gamma(2)} \exp \left[i \frac{\pi}{f\lambda} [(x-x_n)^2 + (y-y_n)^2] \right] + \frac{i\beta}{2\Gamma(2)} \exp \left[-i \frac{\pi}{f\lambda} [(x-x_n)^2 + (y-y_n)^2] \right]
\end{aligned}$$

where we use the relation $J_{-1}(\beta) = J_1(\beta)$. Thus Eq. (3) becomes

$$\begin{aligned}
t(x) & \propto \prod_n \left(1 + \frac{i\beta}{2\Gamma(2)} \exp \left[i \frac{\pi}{f\lambda} [(x-x_n)^2 + (y-y_n)^2] \right] + \frac{i\beta}{2\Gamma(2)} \exp \left[-i \frac{\pi}{f\lambda} [(x-x_n)^2 + (y-y_n)^2] \right] \right) \quad (7) \\
& \approx 1 + \frac{i\beta}{2\Gamma(2)} \sum_n \exp \left[i \frac{\pi}{f\lambda} [(x-x_n)^2 + (y-y_n)^2] \right] + \frac{i\beta}{2\Gamma(2)} \sum_n \exp \left[-i \frac{\pi}{f\lambda} [(x-x_n)^2 + (y-y_n)^2] \right]
\end{aligned}$$

We neglect higher order terms in this analysis. The first term corresponds to the 0 order of the transmitted beam, and the second and third terms correspond to the +1 and -1 order of the diffraction. Comparing with Eq. (1), we can see that the +1 and -1 order diffraction will generate the focus grid and its conjugate image. The amplitude of the +1 order diffraction, which is the diffraction order that we are interested, can be written as

$$\left| \frac{i\beta}{2\Gamma(2)} \right|^2 \propto \beta^2 \propto A_0^2 A_1^2 / f^2 \quad (8)$$

Thus, the reconstructed focus spot intensity will be proportional to the intensity of reference beam, the intensity of sample beam behind the mask, and inversely proportional to the square of focal length. Note that the above equation is an approximation and is not valid for comparable reference and sample beam intensities.

For the focus spot size, a perfectly reconstructed focus spot will be comparable in size to the original aperture in the mask. However, for small apertures that are comparable to the wavelength, the reconstructed spot size will also depend on other factors, such as the resolution of the holographic material, uniformity of the holographic emulsion, the focal length, and the relative intensity between sample and reference beams.

In the next section, we show the result of a series of experiment, where we fabricated holograms using masks with different ODs, different sizes of the apertures, and different focal lengths. The experimental results agree well with the above theoretical analysis.

3. Experiments and Analysis

In the experiment, we used chrome masks with OD = 2.1, 3.2, 4.2, and 5.3. A line of apertures were punched through the metal film on each mask using focused ion beam, and the sizes of the apertures were 0.2, 0.4, 0.6, 0.8, 1.0, 1.2, 1.4, 1.6, 1.8, and 2.0 μm . The separation between adjacent apertures was 60 μm . For each mask, holograms were recorded at focal lengths of $f = 3, 6, 9, 12$ mm. We used a green laser with wavelength of 532 nm and power of 200 mW (Excelsior-532-200, Spectra-Physics) for recording the hologram. The holographic material was silver halide (VRP, Integraf). In the reconstruction, we set the intensity of the collimated beam incident on the hologram to be 17 $\mu\text{W}/\text{cm}^2$.

With increasing ODs, the reference beam was attenuated more and the intensity was closer to that of the sample beam. According to the previous discussion, we should expect to see better diffraction and stronger focus spots for larger OD, since the intensities of the sample beam will be more comparable to that of the reference beam. So it is not surprising that for OD 2.1, and 3.2, the reconstructed spots can be observed clearly for all the aperture sizes except 0.2 μm , and for OD 4.2, all the reconstructed spots can be observed. However, for OD 5.3, we can observe multiple diffractions of the hologram, which prevent a clear correspondence between focus spots and the apertures on the mask.

Figure 2 shows the microscope image of masks and reconstructed spots of holograms with OD 4.2 and OD 5.3. Figure 2(a), 2(b) show the images for OD-4.2 mask, where the reconstructed spots is an exact replication of the apertures. Figure 2(c), 2(d) show the images for OD-5.3 mask, where we can see that the number of reconstructed spots is more than that of the apertures. This is because for OD 5.3, the interference between the transmissions of different apertures is comparable to the interference between the transmission of apertures and the reference beam. Thus unwanted interference between the aperture transmissions would be patterned onto the hologram and prevent a clearly reconstruction of the focus spots that correspond to the original apertures. For OD 2.1, 3.2 and 4.2, the intensity of reference beam is much higher than that of the sample beam, and the correspondence of reconstructed focus spots and original apertures can be clearly seen.

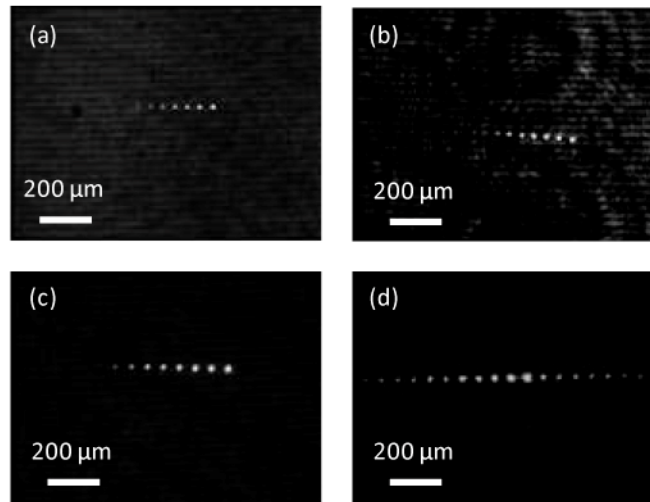


Fig. 2. Microscope image of masks and reconstructed spots of holograms under 4X objective. (a) Mask with OD 4.2; (b) Reconstructed spots of hologram corresponding to OD-4.2 mask; (c) Mask with OD 5.3; (d) Reconstructed spots of hologram corresponding to OD-5.3 mask.

The reconstructed spot intensities and the full-width-half-maximum (FWHM) spot sizes were measured, using a microscope with 60X/NA0.95 objective, for OD 2.1, 3.2, and 4.3 and plotted in Fig. 3, where Fig. 3(a), 3(b) show the plots for OD 2.1, Fig. 3(c), 3(d) show the plots for OD 3.2, and Fig. 3(e), 3(f) show the plots for OD 4.3. From Fig. 3(a), 3(c), and 3(e), we can observe the following important features regarding the reconstructed spot intensity:

- (I1) For same OD and same focal length, the reconstructed spot intensity decreases with smaller aperture size. This could be explained by less transmission through smaller apertures and Eq. (8).
- (I2) The reconstructed spot intensity is roughly inversely proportional to the attenuation coefficient of reference beam through the mask, and thus stronger for larger OD. This is because in the experiment, the total exposure on the holographic plate is set to be the optimal value of $80 \mu\text{J}/\text{cm}^2$ for the holographic material VRP. Assuming that the reference beam intensity is much larger than the sample beam intensity, the increase in OD of the mask will result in increase in sample beam exposure during recording as the exposure time will be longer. Thus according to Eq. (8), the spot intensity will increase to the same amount as OD decreases. The experiment shows that for the same aperture size, the spot intensities of OD-3.2 holograms are roughly 10 times of the spot intensities of OD-2.1 holograms, and the spot intensities of OD-4.2 holograms are roughly 5-8 times of the spot intensities of OD-3.2 holograms. This agrees well with the theory

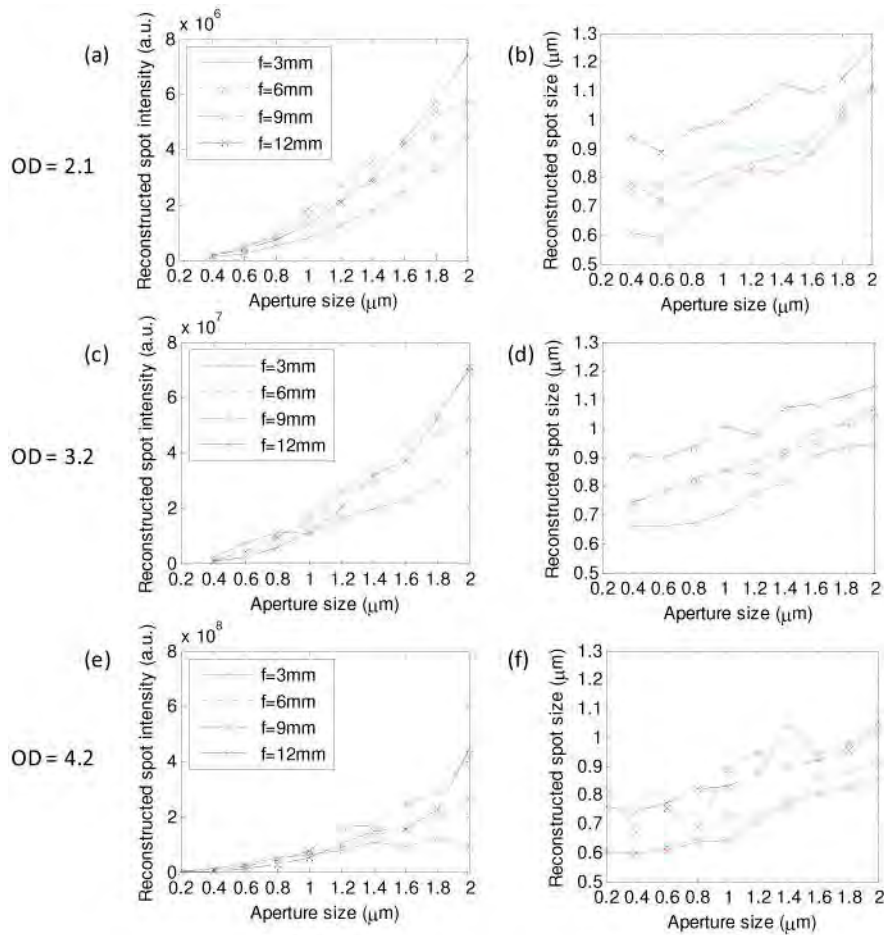


Fig. 3. Reconstructed spot intensity and FWHM spot size versus aperture size at different ODs and different focal lengths. (a)(b) OD = 2.1; (c)(d) OD = 3.2; (e)(f) OD = 4.2.

From Fig. 3(b), 3(d), and 3(f), we can observe the following important features regarding reconstructed spot size:

- (S1) For same OD and same aperture, the spot size decreases with smaller focal length. This could be explained by the effective holographic lens area on the hologram. As the focal length decreases, the effective holographic lens area also decreases, thus the impact of possible non-uniformity of the holographic recording material on the lens quality would be less, and the reconstructed spot size can be closer to the original aperture size.
- (S2) For same OD and same focal length, the spot size decreases with smaller aperture size and finally reaches an asymptotic value. The decrease in spot size is consistent with our logical expectation. The existence of an asymptotic value is unsurprising as well – the holographic material can only record feature size down to a certain limit. Reconstruction of a small spot requires the patterning of finer diffraction features. Once we have reached that limit, we cannot expect the reconstruction spot size to taper to an asymptotic value and any further decrease in the mask's aperture size would have no impact.

We can see that the reconstruction spot can have an FWHM spot size as small as $0.6\ \mu\text{m}$. Note that this can be smaller than the aperture diameter since we measured the FWHM spot size, which was related to the diffraction of the aperture.

(S3) For different OD and same aperture size, we can obtain similar reconstructed spot size, especially for small apertures and small focal lengths. This indicates that the spot size is less sensitive to the relative intensity between reference and sample beam, and more depending on the effective holographic lens area. This implies that the uniformity of the holographic material is an important quality-determining factor.

According to these experimental observations, we can see that to get an optimal hologram quality, we would first need to choose an optimal OD for the mask. An OD of 4 works well for holographic grid designs that are similar to the one we have here. We note that choosing an OD beyond 4 can potentially provide even better efficiency. However, an excessively high OD would significantly attenuate the reference intensity. In our experiments, the direct transmission through the mask becomes exceedingly weak for an OD beyond 5. In this situation, the diffraction transmissions through adjacent apertures would interfere significantly and lead to significant cross-talks.

Next an appropriate aperture size should be chosen according to (I1) and (S2), which show that there is a trade-off between spot intensity and spot size. Finally we can see that for small apertures, the spot intensity and spot size will generally get better as focal length decreases, thus we would want to choose the smallest possible focal length as long as it is compatible with the system design.

In the fabrication of our demonstration focus grid, we chose to use an aperture size of $0.8\ \mu\text{m}$ for small enough reconstructed spot size based on the reasons listed above. Figure 4 shows the reconstructed spot intensity vs. focal length and OD for the $0.8\text{-}\mu\text{m}$ aperture size. We can see that there is an optimal parameter set for getting the best spot intensity.

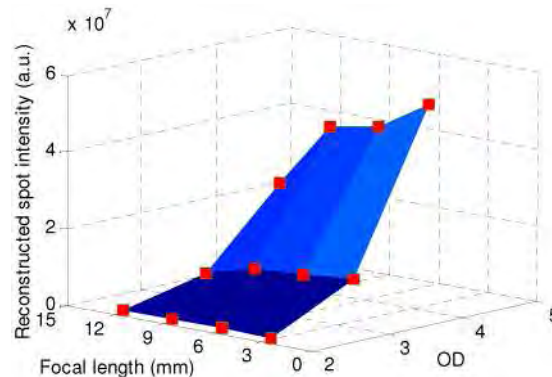


Fig. 4. Reconstructed spot intensity vs. focal length and OD for $0.8\text{-}\mu\text{m}$ aperture size. The squares indicate the experiment data points.

Using the in-line holography method, we fabricated a hologram that can generate a focus grid of 170×138 , with $30\text{-}\mu\text{m}$ separation between the focus spots. The hologram was recorded with an OD 4 mask with apertures of $0.8\text{-}\mu\text{m}$ diameter, and at a focal length of 5 mm. Figure 5 shows a small part of the reconstructed spots observed under microscope with a 20X objective. The FWHM spot size was measured to be around $0.7\ \mu\text{m}$. The focus grid can be readily used in a wide-field microscope system.

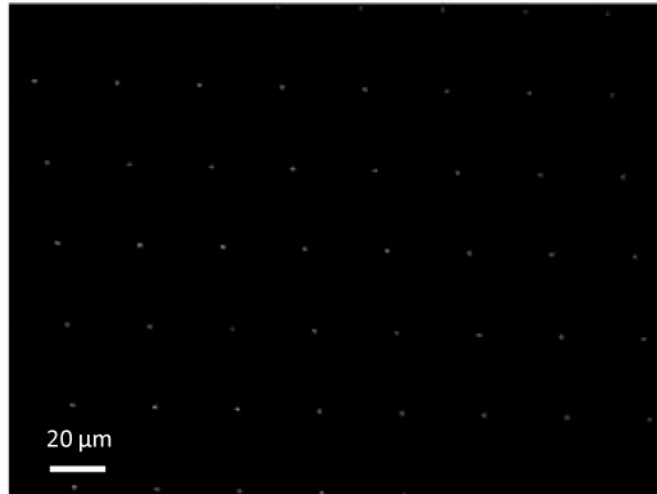


Fig. 5. Microscope image of a small part of the reconstructed focus grid under a 20X objective.

While this set of experiments did not study the impact of aperture separation on the focus grid quality, the observed dependency trends of the other design parameters can help inform us on this relationship. Specifically, an increase in grid density would lead to higher total transmissions through the apertures. This in turn would lead to more interference between the transmissions through different apertures. In this case, we expect a lower OD mask would be required so that the in-line holography interference is stronger than the cross-talk terms. The exact impact of aperture separation is well worth a future detailed experimental study.

4. Summary

In conclusion, we have shown an in-line holography scheme for recording a hologram to generate a wide-area focus grid. Compare with other methods for generating focus grid, our scheme is relatively simple, robust, and have many other advantages. We have studied the effect of mask OD, aperture size, and focal length on recording process and showed that a set of appropriate parameters is important for fabricating the hologram. A hologram was fabricated to generate a wide-area focus grid for demonstration of principle. The hologram can be potentially used for wide field-of-view imaging or parallel detecting and sensing applications.

Acknowledgement

The authors acknowledge Ying Min Wang, Guoan Zheng, and Dr. Xiquan Cui for helpful discussions. This work is supported by Department of Defense grant #W81XWH-09-1-0051.

Focal plane tuning in wide-field-of-view microscope with Talbot pattern illumination

Jigang Wu,^{1,2,*} Guoan Zheng,¹ Zheng Li,¹ and Changhui Yang^{1,3}

¹Department of Electrical Engineering, California Institute of Technology, 1200 East California Boulevard, Pasadena, California 91125, USA

²University of Michigan–Shanghai Jiao Tong University Joint Institute, Shanghai Jiao Tong University, Shanghai 200240, China

³Department of Bioengineering, California Institute of Technology, 1200 East California Boulevard, Pasadena, California 91125, USA

*Corresponding author: jigang@caltech.edu

Received April 15, 2011; accepted May 1, 2011;
posted May 10, 2011 (Doc. ID 145985); published June 6, 2011

We have developed a focal plane tuning technique for use in focus-grid-based wide-field-of-view microscopy (WFM). In WFM, the incidence of a collimated beam on a mask with a two-dimensional grid of aperture produced the Talbot images of the aperture grid. The Talbot pattern functioned as a focus grid and was used to illuminate the sample. By scanning the sample across the focus grid and collecting the transmission, we can generate a microscopy image of the sample. By tuning the wavelength of the laser, we can tune the focal plane of the WFM and acquire images of different depth into the sample. Images of a green algae microscope slide were acquired at different focal planes for demonstration. © 2011 Optical Society of America

OCIS codes: 170.0110, 050.1970, 170.5810.

The ability to collect wide-field-of-view (FOV) microscopic images is highly desired in many applications, such as digital pathology [1] or high-throughput screening [2]. There are numerous recent efforts aimed at addressing this need [3,4]. Previously, we have developed a wide-FOV microscope based on holographic focus grid illumination [5]. In that system, the sample is illuminated with a holographically generated grid of focused light spots, and the transmission of the light spots through the sample is projected onto an imaging sensor by a simple collection optics arrangement. A wide-FOV image can then be acquired by scanning the sample across the focus grid. Unlike conventional microscopy or other multi-beam microscopy [6], the resolution and FOV of such a system are not cross-competing design constraints. Here, the resolution is fundamentally set by the light spot size, and the FOV is set by the size of the holographic grid. As long as the collected light spot transmissions are well separated on the imaging sensor (determined by the spot separation and the collection optics), such a system can perform high-resolution wide-FOV microscopy imaging effectively.

In this Letter we demonstrate an alternate microscope design where the focus grid is generated via the Talbot effect. Here, a mask with an aperture grid is illuminated with a collimated laser beam to produce the focus grid. A “self-image” of the aperture grid will be reproduced at integer increments of the Talbot distance [7]. This focus grid replacement has several advantages. First, the focus grid generation is more repeatable and robust because the mask can be readily fabricated by the microfabrication technique. Second, unlike the holographic method, there is no zero-order transmission of the incident beam in the Talbot effect. This will enhance the contrast of the foci on the sensor and thus the signal-to-noise ratio of the image. Third, the focused light spots are more uniform in their powers (spot-to-spot comparison). Finally, this approach allows us to accomplish z -axis scanning

(focal plane change) by simply tuning the light source wavelength.

This Letter is structured as follows. We will briefly summarize the principle of the Talbot effect and point out certain subtleties that we have to closely consider in adapting the phenomenon for our specific applications. Next, we will describe our experimental setup. We will then report on our demonstration of focal plane tuning and apply the system to perform imaging.

The Talbot effect [8] is a well-known phenomenon in which the transmission from a mask with a periodic grid of apertures will reproduce the grid pattern at regular distance intervals from the mask. The distance interval, termed the Talbot distance Z_T , can be calculated as

$$Z_T = 2d^2/\lambda, \quad (1)$$

where d is the period of the pattern and λ is the wavelength. The periodic pattern will reproduce itself at the distance $Z = mZ_T$ or a phase-reversed image at $Z = (m - 1/2)Z_T$, where m is an integer. In principle, any of these planes can be used as the focus grid for our wide-FOV microscope. In our experiment, we used the second phase-reversed Talbot plane ($Z_{1.5} = 1.5Z_T$) for more convenient experimental setup.

Interestingly, Eq. (1) implies that Z_T is inversely proportional to the wavelength. For small tuning of the wavelength, i.e., $\Delta\lambda \ll \lambda$, the Talbot distance change can be calculated as

$$\Delta Z_T = -2d^2\Delta\lambda/\lambda^2. \quad (2)$$

For a periodicity $d = 30\ \mu\text{m}$ and a nominal wavelength of 700 nm, this implies that we can accomplish a significant plane shift of $55\ \mu\text{m}$ at $Z = Z_{1.5}$ for a small wavelength change of 10 nm. This tuning ability can be used in our microscope design to accomplish the non-mechanical focal plane shift.

As the resolution of our microscopy system depends on the grid spot size generated, the spot size that can be created by the Talbot effect is of importance to us. It is worth noting that the “self-imaging” ability of the Talbot effect is only a paraxial approximation [9]. In other words, the Talbot effect will “self-image” the holes in the mask well only if the hole diameter is much larger than λ [10,11]. The effect will fail and result in “self-image” spots that are substantially larger if the hole diameter is comparable to λ .

As we desire tightly focused light spots for our microscopy application, a straight application of the Talbot effect would not work well. Fortunately, we found that the Talbot field propagation will create tight light spots in planes that are slightly above the Talbot planes. Figures 1(a) and 1(b) show numerical simulations versus experimental characterization of the evolving Talbot patterns around $Z = Z_{1.5, \lambda 1}$ for $\lambda_1 = 702$ nm. Our Talbot mask has a periodicity of $30 \mu\text{m}$ and aperture sizes of 800 nm. Figure 1(a) is the simulation results, and Fig. 1(b) shows experimental spots observed under a conventional microscope with a $60\times$ objective. The simulation was performed by the angular spectrum propagation using Fourier transforms. The Z positions and w , the FWHM, of spots except those in the last column are indicated in the figure. The last column corresponds to $Z = Z_{1.5}$. As we can see, the Talbot effect fails to generate a good focal spot at this position (the self-imaging approximation is not valid for this regime).

We further experimentally imaged the spot pattern at wavelength of $\lambda_2 = 692$ nm [Fig. 1(c)]. It is worth noting that the patterns closely resemble the original set. This is not surprising as the wavelength shift is small. It is further worth noting that the entire pattern set has shifted by a distance of $55 \mu\text{m}$ ($Z = Z_{1.5, \lambda 2} - Z_{1.5, \lambda 1} = 55 \mu\text{m}$) away from the mask. This shift is consistent with the prediction from Eq. (2).

Figure 1 also shows that the light pattern generally consists of a bright central spot and associated concentric rings. As the Z position increases, the center spot gets brighter and larger, while the concentric rings get smaller and finally disappear. By observing the evolving spots, we can see that the best focus spots for imaging are those around $Z_{1.5} - 90 \mu\text{m}$. For smaller z positions, the center spot is too weak for a good contrast imaging. While for larger Z positions, the center spot is too large to provide high-resolution images. The observed spots

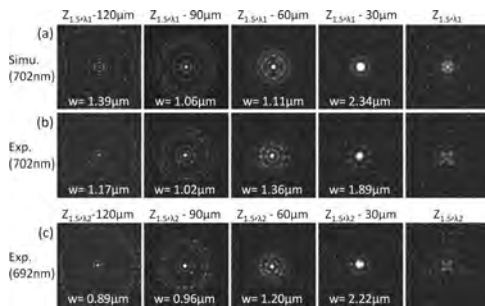


Fig. 1. Evolving of Talbot patterns around $Z = Z_{1.5}$. (a) Simulation spots for $\lambda_1 = 702$ nm. (b) Spots for $\lambda_1 = 702$ nm. (c) Spots for $\lambda_2 = 692$ nm. w is the FWHM spot size, and $Z_{1.5, \lambda 2} - Z_{1.5, \lambda 1} = 55 \mu\text{m}$. The size of each pattern figure is $30 \mu\text{m} \times 30 \mu\text{m}$.

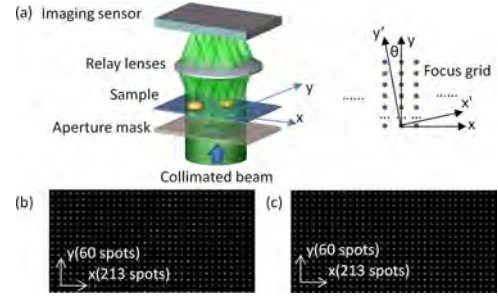


Fig. 2. (Color online) (a) Experimental setup of the wide-FOV microscope based on the Talbot illumination. (b) Part of the aperture grid on the mask plane. (c) Part of the focus grid at $Z = Z_{1.5}$. The number of spots along the x and y directions for the full mask is indicated.

show that we can get a resolution of $\sim 1 \mu\text{m}$, which was verified by acquiring images of a United States Air Force (USAF) target in the experiment.

Our experimental setup is shown in Fig. 2(a). An aperture mask was illuminated by a collimated beam introduced from a tunable Ti:sapphire laser (Spectra-Physics). As mentioned earlier, we employed an aperture mask with periodicity of $d = 30 \mu\text{m}$ and aperture size of 800 nm. The laser wavelength was tuned from 692 to 702 nm to vary the Talbot distance. The distance between the mask and the sample was set at $Z = Z_{1.5}$ during initial alignment. We subsequently fine-tuned the distance to make use of the tighter light spots discussed in the previous paragraph.

According to Eq. (2), the tuning range of the focal plane position was $55 \mu\text{m}$ in the experiment. Similar to the setup in our previous paper [3], the sample was illuminated by the focus grid and the transmission of the foci was projected by relay lenses (NT45-760, Edmund Optics, Inc.) onto an imaging sensor (LuCam080M, Lumenera Corp.). The sample was scanned across the focus grid and the scanning direction (y' direction) was slightly tilted at a small angle θ with respect to the focus grid, which was oriented at the x and y directions. The image can be reconstructed by combining line scans from each focal spots and properly shifting each line according to the scanning speed.

Figures 2(b) and 2(c) show part of the aperture grid on the mask plane and part of the focus grid at $Z = Z_{1.5}$, respectively. We can see that the intensity uniformity of the focus grid is better than the original aperture grid. The averaged relative adjacent spot intensity variation is 4% for the focus grid and 20% for the original aperture grid. This is reasonable, because many apertures will contribute to a focal spot; thus, the intensity difference of the original aperture grid will be partially averaged out. During image processing, we further ensure image uniformity by normalizing each scan line to compensate for the nonuniformity intensity distribution of the focal spots in the experiment.

We next used our system for imaging demonstration. The focus grid we used has 213×60 (in the x and y directions, respectively) spots, and the scanning was performed along the y' direction. Thus the reconstructed image is oriented at the x' and y' directions. The image will have a sawtooth shape at the starting and ending part because of the linear scanning characteristics.

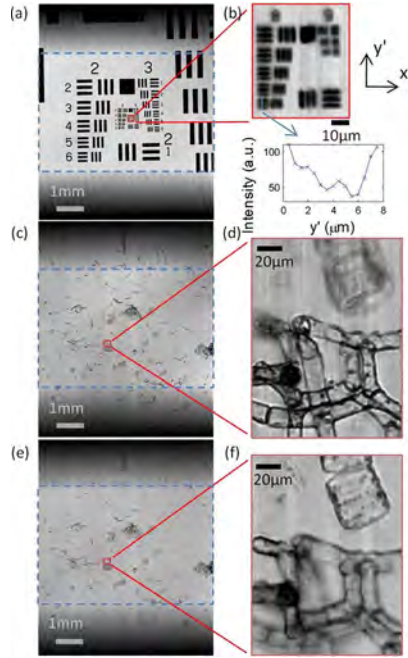


Fig. 3. (Color online) Images acquired by the Talbot wide-FOV microscope with an effective FOV of $6.4\text{ mm} \times 4.2\text{ mm}$. (a) Wide-FOV image of a USAF target, with effective FOV indicated in the large dashed rectangle. (b) Expanded view of the smallest feature of the target and cross-sectional profile of group 8, element 6. (c) Wide-FOV image of a mixed green algae slide with $\lambda = 692\text{ nm}$, with effective FOV indicated in the large dashed rectangle. (d) Expanded view of the region indicated in (c). (e) Wide-FOV image of a mixed green algae slide with $\lambda = 702\text{ nm}$, with effective FOV indicated in the large dashed rectangle. (f) Expanded view of the region indicated in (e).

The effective FOV in x' direction is $213^\circ d \approx 6.4\text{ mm}$. In the experiments, the sample was moved at a speed of $v = 0.165\text{ mm/s}$ for $L = 6\text{ mm}$. At the same time, the imaging sensor acquired 12,000 frames at $F = 330\text{ frames/s}$. The exposure time of the sensor was 0.5 ms . Thus, the sampling distance in the y' direction is $v/F = 0.5\text{ }\mu\text{m}$. The sampling distance in the x' direction is determined by the angle θ between the scanning direction (y' direction) and the grid orientation (y direction), which was set to be 0.0167 . Thus the sampling distance in x' direction is $d^* \sin(\theta) = 0.5\text{ }\mu\text{m}$. The effective FOV in the y' direction can be calculated by $L - H = 4.2\text{ mm}$, where $H = 60^\circ d = 1.8\text{ mm}$ is the extent of the focus grid in the y direction.

For the resolution test, we first image a USAF target, as shown in Figs. 3(a) and 3(b). Figure 3(a) is a wide-FOV image ($6.4\text{ mm} \times 4.2\text{ mm}$), and Fig. 3(b) is the expanded view of the region indicated in Fig. 3(a). The cross-sectional profile of group 8, element 6 is also shown in the figure. We can see that features sized with a line

width of $1.1\text{ }\mu\text{m}$ (group 8, element 6) can be resolved, which agrees with the measured spot size of $\sim 1\text{ }\mu\text{m}$ as shown in Fig. 1.

We then acquired images of a mixed green algae microscope slide (Carolina Biological Supply Company). Images were acquired at different focal planes, where Fig. 3(c) is for $\lambda = 692\text{ nm}$ and Fig. 3(e) is for $\lambda = 702\text{ nm}$. Figures 3(d) and 3(f) show the expanded view of corresponding regions indicated in Figs. 3(c) and 3(e), respectively. We can see that Figs. 3(d) and 3(f) were focusing at different focal planes and were able to render high-resolution images of the sample at different planes.

At this point, it is worth noting that it is unclear if this Talbot illumination approach can provide resolution better than $1\text{ }\mu\text{m}$. It may be possible to design the aperture geometry to diffract more light at large angles to help in tighter focus spot generation. The spot quality will also be degraded for thick scattering samples, especially when the focus spot is tighter.

In summary, we report a wide-FOV microscope based on Talbot pattern illumination. The wavelength of the laser source can be tuned to change the focal plane distance in order to obtain images at different focal planes. The elimination of mechanical scanning along the focal axis can be a significant advantage for fast scanning microscopy applications. The focal spot size was measured to be $\sim 1\text{ }\mu\text{m}$ under a conventional microscope. Images of a USAF target and a mixed green algae microscope slide with an FOV of $6.4\text{ mm} \times 4.2\text{ mm}$ are acquired for demonstration of the system.

This work is supported by the United States Department of Defense under grant W81XWH-09-1-0051. The authors acknowledge Richard Cote and Ram Datar from the University of Miami for helpful discussions.

References

1. J. Ho, A. V. Parwani, D. M. Jukic, Y. Yagi, L. Anthony, and J. R. Gilbertson, *Hum. Pathol.* **37**, 322 (2006).
2. M. Oheim, *Br. J. Pharmacol.* **152**, 1 (2007).
3. W. Bishara, T. W. Su, A. F. Coskun, and A. Ozcan, *Opt. Express* **18**, 11181 (2010).
4. M. G. Rojo, G. B. Garcia, C. P. Mateos, J. G. Garcia, and M. C. Vicente, *Int. J. Surg. Pathol.* **14**, 285 (2006).
5. J. Wu, X. Cui, G. Zheng, Y. M. Wang, L. M. Lee, and C. Yang, *Opt. Lett.* **35**, 2188 (2010).
6. R. Graf, J. Rietdorf, and T. Zimmermann, *Adv. Biochem. Eng. Biotechnol.* **95**, 1311 (2005).
7. J. R. Leger and G. J. Swanson, *Opt. Lett.* **15**, 288 (1990).
8. H. F. Talbot, *Philos. Mag.* **9**, 401 (1836).
9. K. Paturski, *Prog. Opt.* **27**, 1 (1989).
10. B. Besold and N. Lindlein, *Opt. Eng.* **36**, 1099 (1997).
11. E. di Mambro, R. Haidar, N. Guerinneau, and J. Primot, *J. Opt. Soc. Am. A* **21**, 2276 (2004).

0.5 gigapixel microscopy using a flatbed scanner

Guoan Zheng,* Xiaoze Ou, and Changhuei Yang

*Department of Electrical Engineering, California Institute of Technology, Pasadena, CA
91125, USA*

**gazheng@caltech.edu*

Abstract: Microscopy imaging systems with a very wide field-of-view (FOV) are highly sought in biomedical applications. In this paper, we report a wide FOV microscopy imaging system that uses a low-cost scanner and a closed-circuit-television (CCTV) lens. We show that such an imaging system is capable to capture a 10 mm * 7.5 mm FOV image with 0.77 micron resolution, resulting in 0.54 gigapixels (10^9 pixels) across the entire image (26400 pixels * 20400 pixels). The resolution and field curve of the proposed system were characterized by imaging a USAF resolution target and a hole-array target. Microscopy image of a blood smear and a pathology slide was acquired by using such a system for application demonstration.

©2011 Optical Society of America

OCIS codes: (170.0110) Imaging systems; (170.4730) Optical pathology; (170.0180) Microscopy

References and links

1. M. Oheim, "Advances and challenges in high-throughput microscopy for live-cell subcellular imaging," *Expert Opinion on Drug Discovery*, 1-17 (2011).
2. A. VanderLugt, *Optical signal processing* (Wiley New York, 1992).
3. J. Gilbertson, J. Ho, L. Anthony, D. Jukic, Y. Yagi, and A. Parwani, "Primary histologic diagnosis using automated whole slide imaging: a validation study," *BMC clinical pathology* 6, 4 (2006).
4. <http://www.dmetrix.net/techtutorial1.shtml>.
5. G. Zheng, S. A. Lee, Y. Antebi, M. B. Elowitz, and C. Yang, "The ePetri dish, an on-chip cell imaging platform based on subpixel perspective sweeping microscopy (SPSM)," *Proceedings of the National Academy of Sciences* 108, 16889-16894 (2011).
6. W. Bishara, T. Su, A. Coskun, and A. Ozcan, "Lensfree on-chip microscopy over a wide field-of-view using pixel super-resolution," *Optics Express* 18, 11181-11191 (2010).
7. J. Wu, X. Cui, G. Zheng, Y. M. Wang, L. M. Lee, and C. Yang, "Wide field-of-view microscope based on holographic focus grid illumination," *Optics letters* 35, 2188-2190 (2010).
8. J. Wu, G. Zheng, Z. Li, and C. Yang, "Focal plane tuning in wide-field-of-view microscope with Talbot pattern illumination," *Optics letters* 36, 2179-2181 (2011).
9. J. Di, J. Zhao, H. Jiang, P. Zhang, Q. Fan, and W. Sun, "High resolution digital holographic microscopy with a wide field of view based on a synthetic aperture technique and use of linear CCD scanning," *Applied optics* 47, 5654-5659 (2008).
10. M. Lee, O. Yaglidere, and A. Ozcan, "Field-portable reflection and transmission microscopy based on lensless holography," *Biomedical Optics Express* 2, 2721-2730 (2011).
11. K. Fife, A. Gamal, and H. Wong, "A 3mpixel multi-aperture image sensor with 0.7 um pixels in 0.11 um cmos," in *IEEE ISSCC Digest of Technical Papers*, (2008), 48-49.
12. M. Ben-Ezra, "Large-Format Tile-Scan Camera," *IEEE Computer Graphics and Applications*, 49-61 (2011).
13. S. Wang and W. Heidrich, "The Design of an Inexpensive Very High Resolution Scan Camera System," *Computer Graphics Forum* 23, 441-450 (2004).
14. S. A. Lee, R. Leita, G. Zheng, S. Yang, A. Rodriguez, and C. Yang, "Color Capable Sub-Pixel Resolving Optofluidic Microscope and Its Application to Blood Cell Imaging for Malaria Diagnosis," *PloS one* 6, e26127 (2011).
15. J. Mallon and P. F. Whelan, "Calibration and removal of lateral chromatic aberration in images," *Pattern recognition letters* 28, 125-135 (2007).
16. http://www.linhofstudio.com/products/cameras/anagramm_digital_reproduction/anagramm_digital_reproduction.html.
17. G. Zheng, C. Kolner, and C. Yang, "Microscopy refocusing and dark-field imaging by using a simple LED array," *Optics letters* 36, 3987-3989 (2011).

1. Introduction

The conventional microscope architecture can be generally defined as consisting of a microscope objective for light collection from a sample slide, intermediate relay optics and a pair of or a singular eyepiece that projects a magnified image of the sample into our eyes. With the advancement of digital cameras, the eyepiece(s) segment of the microscope has undergone adaptation changes to be replaced with appropriate optics and camera to enable electronic imaging. Over the past decades and with the broad acceptance of infinity correction, the conventional microscope design has achieved extensive standardization across the microscopy industry - objectives and eyepieces from the major microscope makers are largely interchangeable. This standardization helps with cost-effectiveness. However, it has also limited the commercial design space for conventional microscopy - any significant design deviation that exceeds the standardization parameter space would have to contend with its incompatibility with the entrenched microscopy consumer base.

Recently, there has been an increased recognition that bioscience and biomedical microscopy imaging needs are outstripping the capability of the standard microscope. One salient need of modern bioscience and biomedical community is for a microscopy imaging method that is able to electronically acquire a wide field-of-view (FOV) image with high resolution [1]. The standard microscope was originally designed to provide sufficient image details to a human eye or a digital camera sensor chip. As an example, the resolution of a conventional 20X objective lens (0.4 numerical aperture) is about $0.7\text{ }\mu\text{m}$ and the FOV is only about 1 mm in diameter. The resulting space-bandwidth-product (SBP) [2] is about 8 megapixels (the number of independent pixels to characterize the captured image). This pixel count has only been recently reached or exceeded by digital camera imager. Interestingly, this SBP shows only slight variation across the range of commercial microscope objectives. Placed in different context, the relative invariance of SBP necessarily ties resolution and FOV together for most commercial objectives - high-resolution imaging necessarily implies a limited FOV.

In the past years, there has been significant progress in the development of system that increases the FOV of the conventional microscope system by incorporating sample slide scanning to acquire image over a large area [3] or by implementing parallel imaging with multiple objectives [4]. In addition, there have also been exciting research efforts into wide FOV imaging system, including ePetri dish [5], digital in-line holography [6], focus-grid scanning illumination [7, 8], off-axis holography microscopy [9, 10]. All these methods try to break the tie between resolution and FOV by abandoning the conventional microscopy design and shifting away from the use of optics schemes that perform optical image magnification.

The underlying assumptions that underpin all of these developments appear to be 1) a higher SBP (order of magnitude or more) with a magnification-based optical scheme is commercially impractical and 2) the associated pixel count for a radically higher SBP would face electronic image acquisition issues for which a viable solution does not yet exist.

In this paper, we demonstrate an optical magnification microscopy solution that challenges these assumptions. The configuration of this imaging system is based on two cost-effective items: a commercial available closed-circuit-television (CCTV) lens system and a low-cost consumer flatbed scanner. We show that, such a system is capable to capture a 0.54 gigapixel microscopy image with a FOV of $10\text{ mm} \times 7.5\text{ mm}$ and that a 0.77 resolution is achieved across the entire FOV. Remarkably, the CCTV lens system has a SBP of at least 0.5 gigapixel (10^9 pixels), which is about 2 orders of magnitude larger than those of conventional microscope objectives.

This paper is structured as follows: we will first present our proof-of-concept setup; then, we will present the automatic focusing scheme of the platform. Next, we will report on the resolution and the field-curve characterization of the platform. Then, we will demonstrate the application of the proposed setup by imaging a blood smear and a pathology slide; finally, we

will discuss some limitations as well as future directions for the proposed gigapixel microscopy system.

2. The prototype setup of the 0.5 gigapixel microscopy imaging system

Driven by the recent trend of small pixel size of the image sensor ($0.7\mu\text{m}$ pixel size has been reported in Ref. [11]), significant efforts have been put into the design of consumer/industry camera lens to match this diffraction-limited pixel size. In the past years, it has been demonstrated that the SBP of some consumer camera lenses can achieve count on the order of billion pixels, i.e. these camera lenses are capable to capture gigapixel images [12, 13].

In our proposed microscopy imaging system, we redirected this gigapixel imaging effort [12, 13] to microscopy. The main component of the setup was a commercial available high-quality CCTV lens (C30823KP, Pentax, $f/1.4$, focal length 8mm). Like other consumer/industry camera lenses, the conventional use of this lens is to demagnify the scene onto the image plane, where the CMOS/CCD imager is located. In our setup (Fig. 1), we put our sample at the image plane to replace the CMOS/CCD imager and used the CCTV lens to magnify the sample, i.e. using the lens in the reverse manner. With a magnification factor of ~ 30 , the projected image was too large to be directly imaged with a CMOS/CCD imager. Instead, we modified and employed a consumer flatbed scanner (Canon LiDE 700F) to accomplish image acquisition. We chose this scanner for two reasons: 1) its “LED Indirect Expose (LiDE)” design and 2) the high scanning resolution (2400 dpi is measured, corresponding to a $10\mu\text{m}$ pixel size of the scanner). Due to its LiDE design, this scanner actually possesses a linear CCD that covers the complete width of the scanning area. In comparison, other conventional scanners use a combination of mirrors and lenses to accomplish the same functionality, and it will take additional steps to modify these scanners for our application. In our setup, we disabled the LED light source of the Canon LiDE 700F scanner by using a black tape. The relay lens array and the light guide on top of the linear CCD were also removed. Therefore, the linear CCD shown in Fig. 1 was directly exposed to the projected image from the CCTV lens.

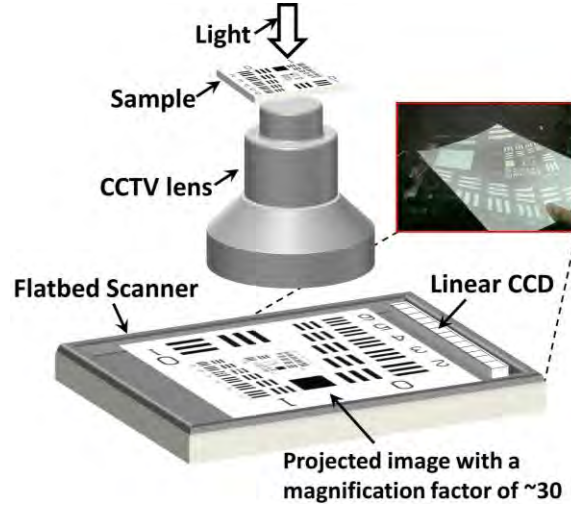


Fig. 1. The setup of the proposed 0.54 gigapixel microscopy (not to scale). A CCTV lens is used to magnify the sample by a factor of 30 and a scanner is used to capture the projected image. The distance between the sample and the lens is about 1 cm. Inset on the top right shows the magnified image of a USAF target on an A4 paper held in front of the scanner.

The scanning resolution was set to 2400 dpi, the maximum resolution of the scanner (corresponds to a $10\mu\text{m}$ pixel size); the FOV of the scanner was set to the maximum scanning area ($297\text{ mm} \times 216\text{ mm}$). The magnification factor was ~ 30 in our platform, and it corresponded to a FOV of $10\text{ mm} \times 7.5\text{ mm}$ at the object side. The distance between the

sample and the CCTV lens is about 1 cm and the distance between scanner and the lens is about 30 cm. We used a diffuse LED light source from top for illumination. Based on these settings, the capture image contained 26400 pixels * 20400 pixels, and thus, it produced a 0.54 gigapixel microscopy image of the sample. Inset of Fig.1 shows the projected image of a USAF target on a letter size paper held in front of the scanner.

3. Automatic focusing scheme

In a conventional microscope setup, the image recording device can give real time update on the object, and therefore, it is easy to adjust the position of the stage to the best focus position. In the proposed platform, the scanner takes a relative long time to acquire the entire image of the object, and thus, it takes a long time to find out the best focus position. To address this issue, we used an automatic focusing scheme with a programmable stage in our setup, as shown in the inset of Fig. 2(a2). This focusing scheme consists of three steps: 1) move the stage with a constant speed (5 $\mu\text{m/s}$); 2) acquire the image at the same time (only certain part of the image is in-focus along the scanning direction); 3) define an F index to find out the best focus position from the acquire image. In step 3, we define the F index using the following equation

$$F \text{ index} = \sum_{x=1}^{\text{end}} |2f(x, y) - f(x - \text{step}, y) - f(x + \text{step}, y)| \quad (1)$$

Such an F index is a measurement of the sharpness of the image.

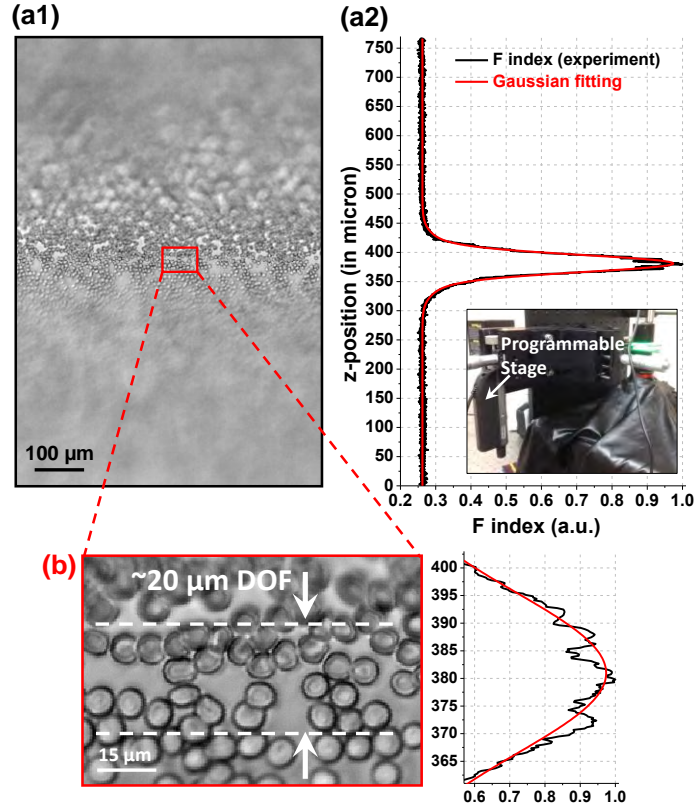


Fig. 2. The automatic focusing scheme of the proposed setup. (a1) The acquired image of a blood smear with the stage moving at a constant speed at z-direction. (b) Based on the motion speed, we can plot the F index with respect to different z positions, and thus, automatically locate the best focused position of the sample. (b) The magnified image of (a), where the depth-of-focus is estimated to be $\sim 20 \mu\text{m}$. In this experiment, a diffused green LED with 20 nm spectrum bandwidth is used for illumination.

Fig. 2(a1) is the acquired image of a blood smear following the above steps (only a small portion of the image is acquired for faster scanning). We can see that the sample is out-of-focus at the beginning, then, the stage bring the sample into focus at the middle part of the image, and finally, the sample is out-of-focus again. Based on the motion speed of the programmable stage, we can plot the F index (with 'step'=2) versus different z-positions, as shown in Fig. 2(a2). The peak of the F index is estimated to be located at $z=381\text{ }\mu\text{m}$. The magnified image and the corresponding F index are shown in Fig. 2(b), where the depth-of-focus (DOF) is estimated to be $\sim 20\text{ }\mu\text{m}$. The proposed automatic focusing scheme works well with biological samples and pathology slides. The entire focusing process takes about 1~2 minutes for the proposed platform. However, we note that, if the sample is extremely sparse (for example, one small hole on a metal mask), such a scheme will fail and we have to take multiple images at different z positions to find out the best focus position.

4. The resolution and the field curve of the platform

We next characterize the resolution and the field-curve of the proposed imaging system. We first imaged a USAF target, as shown in Fig. 3. It is well known that, the aberration of a physical lens will degrade the image resolution at different FOVs of the lens, i.e. the resolution may be different from the center to the edge FOVs. In order to test the resolution at different FOVs, we translated the USAF target across the FOV of the CCTV lens and captured the corresponding images in Fig. 3(a-c). A diffused green LED light source (530 nm wavelength, with $\sim 20\text{ nm}$ spectrum bandwidth) was used in this experiment for illumination.

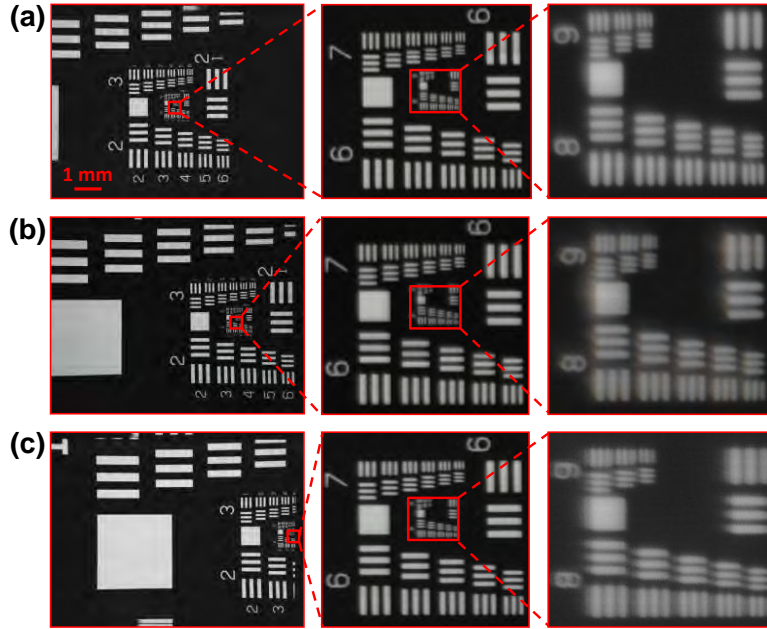


Fig. 3. USAF resolution target acquired by the proposed 0.54 gigapixel microscopy system. The effective FOV is about $10\text{ mm} \times 7.5\text{ mm}$, with $26400\text{ pixels} \times 20400\text{ pixels}$ across the entire image. The imaging performance at the (a) center, (b) 50% away from center and (c) 95% away from center. The line widths of group 9, element 1, 2 and 3 are $0.98\text{ }\mu\text{m}$, $0.87\text{ }\mu\text{m}$ and $0.77\text{ }\mu\text{m}$ respectively.

In the USAF target, the line widths of group 9, element 1, 2 and 3 are $0.98\text{ }\mu\text{m}$, $0.87\text{ }\mu\text{m}$ and $0.77\text{ }\mu\text{m}$ respectively. The image performance at the center of the FOV is shown in Fig. 2(a), where we can clearly see the feature at group 9, element 3 ($0.77\text{ }\mu\text{m}$ line width). In Fig. 2(b) and (c), we translate the sample to 50% and 95% of the FOV away from center (100% corresponds to 10 mm). In both images, we can still clearly see the fine feature at group 9, element 3 ($0.77\text{ }\mu\text{m}$ line width). This establishes the resolution of our prototype system is,

under the monochromatic green light illumination, $0.77\ \mu\text{m}$ over the entire FOV. We note that, by Nyquist theorem, we need at least two pixels to capture the smallest detail of the image, and thus, the effective pixel size at the object size should be less than $385\ \text{nm}$. Based on section 1, the effective pixel size of our platform is about $330\ \text{nm}$ ($10\ \mu\text{m}$ divided by magnification factor), which fulfills the requirement of Nyquist theorem in this regard. In Fig. 3(c), the horizontal resolution is worse than the vertical resolution. Such an effect is due to the high order aberration of the lens, such as coma. We also note that, due to the pixel-response differences of the linear CCD, line-artifact is present in the raw scanning data [13]. This effect can be eliminated by performing a simple normalization process: 1) capture a reference image without any sample; 2) normalized the raw scanning image of the sample with the reference image. In this process, the reference image is sample-independent, i.e., it can be used for any sample.

In the second experiment, we want to characterize the field curve of the imaging system. Our sample was a chrome mask ($1.8\ \text{cm} \times 1.8\ \text{cm}$) with a hole-array on it (fabricated by lithography). The size of the hole was about $1\ \mu\text{m}$ in diameter and periodicity of the hole-array was $30\ \mu\text{m}$. The light source of this experiment is the same as before (a green LED with a $20\ \text{nm}$ spectrum bandwidth). First, we captured a series of images as we mechanically shifted the chrome mask into different z positions; then, we analyzed the spot size to locate the best focal plane for different FOVs, with the result shown in Fig. 4 (for example, at 50% FOV, the best focal plane locates at $z = 6\ \mu\text{m}$). The displacement of the best focal plane is directly related to field curve of the imaging system. Remarkably, the result shows that the field curvature is relatively small (maximum observed of $12\ \mu\text{m}$ z -displacement) over the entire FOV under the monochromatic illumination.

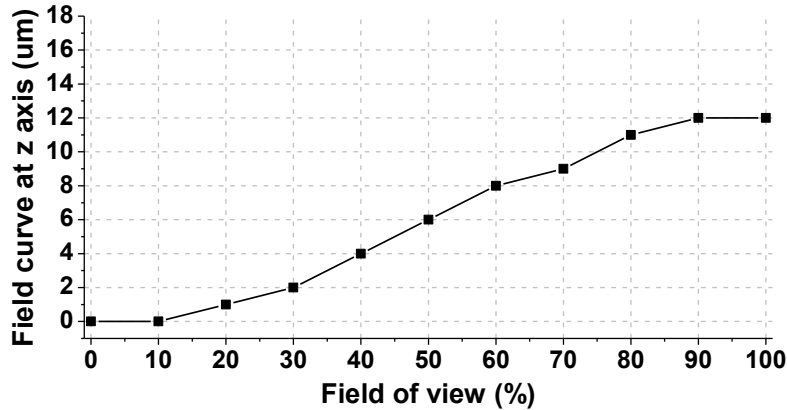


Fig. 4 Displacement of the best focal plane of different FOVs (from center to edge FOV). In this figure, 100% in x-axis corresponds to $10\ \text{mm}$.

5. Imaging of a blood smear and a pathology slide

We next used our system for imaging demonstration. First, we acquired a monochromatic image of a human blood smear using a green LED light source. The sample was automatically tuned to its in-focus position based on the automatic focusing scheme described in Section. 2. Fig. 5 shows the acquired image, where the scanner and magnification setting is the same as before. There are 200 times difference in the scale bars between Fig. 5(a) and (b3). In order to appreciate the wide FOV capability, we also prepare a video showing the entire and the magnified view of the image ([Media 1](#)).

The proposed platform can also be used for color imaging. We used R/G/B diffused LED light sources for three color illuminations, similar to Ref. [14]. The sample slide was automatically tuned into its in-focus position for each color illumination ($\Delta z = 3\ \mu\text{m}$ for the blue LED and $-12\ \mu\text{m}$ for the red LED). Three images (for R/G/B) are separately acquired, normalized, aligned [15] and then combined into the final color image. Fig. 6 shows the

acquired color image of a pathology slide (human metastatic carcinoma to liver, Carolina Biological Supply). Fig. 6(a) shows the wide FOV image of the pathology sample. Fig.6 (b1), (b2) and (c1), (c2) are the corresponding expanded view for Fig. 6(a).

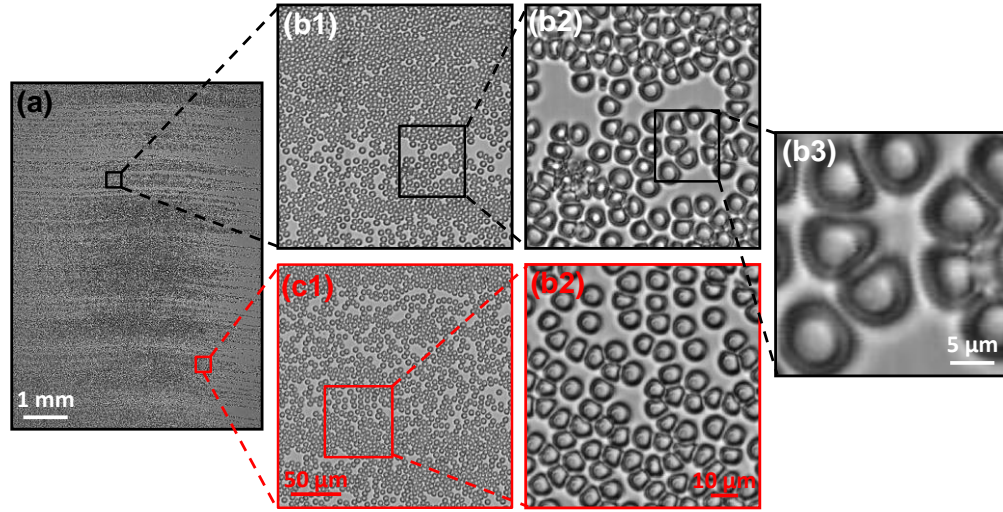


Fig. 5 ([Media 1](#)) 0.54 monochromatic gigapixel image of a blood smear. (a) The full frame of the captured image. (b1), (b2), (b3) and (c1), (c2) are the expanded view of the (a).

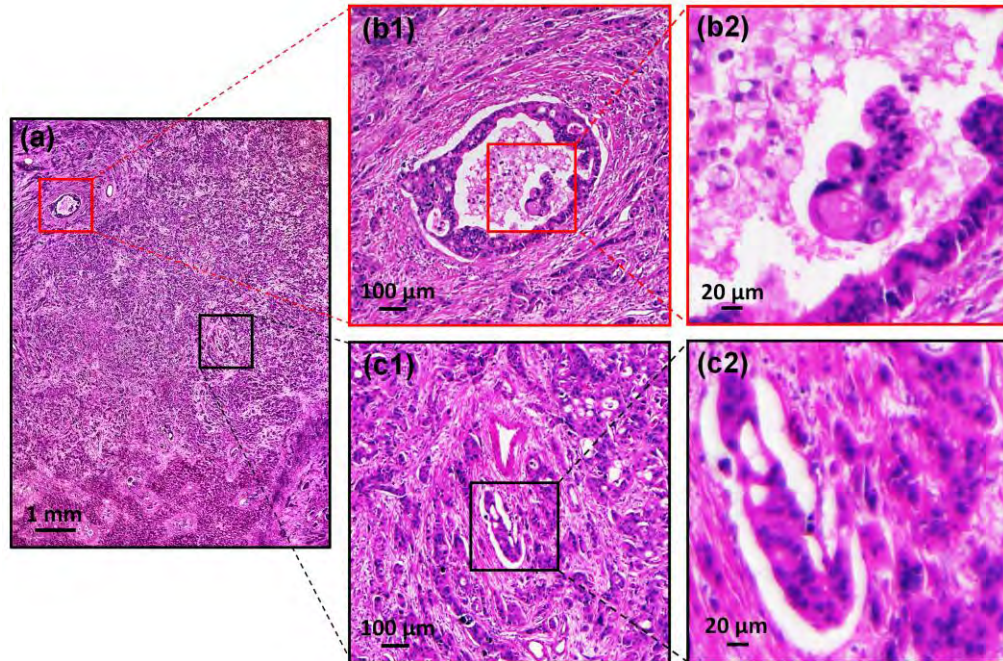


Fig. 6 0.54 gigapixel color image of a pathology slide (human metastatic carcinoma to liver). (a) The full frame of the acquired image. (b1), (b2) and (c1), (c2) are the expanded view of (a).

6. Conclusion

In summary, we report a wide-FOV (10 mm * 7.5 mm) microscopy system which can generate a 0.54 gigapixel microscopy image with 0.77 μm resolution across the entire FOV.

We note that there are other large-format professional camera lenses for even larger FOV (for example, 35 mm in diameter). The bottom line we want to convey in this paper is that lenses from the photography/industry community may provide a potential solution for high throughput microscopy imaging. Interested readers can choose their lenses based on the balance between the price and the performance.

It is interesting to contrast the SBP and resolution of our demonstrated system versus those of the conventional microscope. As shown in Fig. 7, the effective SBP of our system is more than one order of magnitude greater than those of the microscope objectives. Compared to a typical 10X and 4X objectives, our system has both superior SBP and resolution.

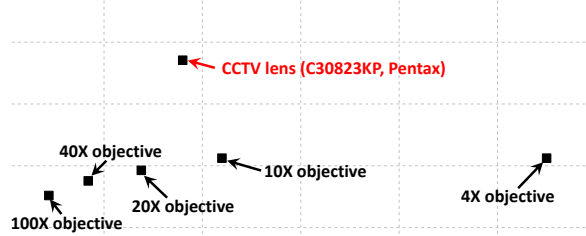


Fig. 7 The SBP-resolution summary for microscope objectives and the proposed system.

We note that one important limitation of the system is the scanning speed. A full-scan at 2400 dpi scanning resolution with USB 2.0 link took about 10 minutes. There are three strategies to address this issue: 1) use other high speed scanners; 2) use multiple scanners for parallelization (we can take out the linear CCDs and its housing components from multiple scanners and assemble them into one scanner); 3) use other scanning devices such as the digital scanning back (for example, a commercial available digital scanning back takes 29 seconds to capture a 0.312 gigapixel image [16]). Our future directions include: 1) improve the speed of setup using the strategies discussed above; 2) incorporate other imaging functionalities such as 3D, darkfield and phase imaging into the proposed wide FOV platform [17, 18].

Acknowledgements

We are grateful for the constructive discussions and generous help from Mr. Roarke Horstmeyer, Dr. Jigang Wu, and Mr. Zheng Li from Caltech. We acknowledge funding support from the United States Department of Defense under grant W81XWH-09-1-0051.